EFFICIENCY OF $CH_3NH_3Pb(SCN)_xI_{3-x}$ FILMS AS LIGHT-ABSORBER IN CARBON-BASED HOLE-TRANSPORT-LAYER-FREE PEROVSKITE SOLAR CELLS

PRIMPRAPHA PRASAN

Graduate School Srinakharinwirot University

2021

ประสิทธิภาพฟิล์ม $CH_3NH_3Pb(SCN)_xI_{3-x}$ ที่ใช้สำหรับชั้นดูดกลืนแสงในระบบเซลล์แสงอาทิตย์ชนิดเพอรอฟสไกต์ที่ไม่มีชั้นนำส่งโฮลและใช้ฟิล์มคาร์บอนเป็นขั้วนำไฟฟ้า

ปริมประภา ปราสาร

ปริญญานิพนธ์นี้เป็นส่วนหนึ่งของการศึกษาตามหลักสูตร
การศึกษามหาบัณฑิต สาขาวิชาฟิสิกส์
คณะวิทยาศาสตร์ มหาวิทยาลัยศรีนครินทรวิโรฒ
ปีการศึกษา 2564

EFFICIENCY OF $CH_3NH_3Pb(SCN)_xI_{3-x}$ FILMS AS LIGHT-ABSORBER IN CARBON-BASED HOLE-TRANSPORT-LAYER-FREE PEROVSKITE SOLAR CELLS

PRIMPRAPHA PRASAN

A Thesis Submitted in Partial Fulfillment of the Requirements
for the Degree of MASTER OF EDUCATION
(Physics)
Faculty of Science, Srinakharinwirot University
2021

THE THESIS TITLED

EFFICIENCY OF $CH_3NH_3PB(SCN)_XI_{3-X}$ FILMS AS LIGHT-ABSORBER IN CARBON-BASED HOLE-TRANSPORT-LAYER-FREE PEROVSKITE SOLAR CELLS

BY
PRIMPRAPHA PRASAN

HAS BEEN APPROVED BY THE GRADUATE SCHOOL IN PARTIAL FULFILLMENT
OF THE REQUIREMENTS FOR THE MASTER OF EDUCATION
IN PHYSICS AT SRINAKHARINWIROT UNIVERSITY

(Assoc. Prof. Dr. Chatchai Ekpanyaskul, MD.)
Dean of Graduate School

ORAL DEFENSE COMMITTEE

.... Major-advisor
(Assoc. Prof. Dr.Samuk Pimanpang)

.... Chair
(Assoc. Prof. Dr.Chesta Ruttanapun)

.... Committee
(Asst. Prof. Dr.Chokchai Puttharugsa)

Title EFFICIENCY OF $CH_3NH_3Pb(SCN)_xI_{3-x}$ FILMS AS LIGHT-ABSORBER IN
CARBON-BASED HOLE-TRANSPORT-LAYER-FREE
PEROVSKITE SOLAR CELLS
Author PRIMPRAPHA PRASAN
Degree MASTER OF EDUCATION
Academic Year 2021
Thesis Advisor Associate Professor Dr. Samuk Pimanpang

The $CH_3NH_3Pb(SCN)_xI_{3-x}$ perovskite films were prepared via the hot-casting method. The surface morphology of $CH_3NH_3Pb(SCN)_xI_{3-x}$ perovskite films with low SCN^- dopant levels ($x = 0.0625$ to $x = 0.1875$) showed smooth surfaces. However, with high SCN^- dopant levels (at $x = 0.25$ and $x = 0.5$), rough surfaces with pinholes were produced. The crystal of pure $CH_3NH_3PbI_3$ ($x = 0$) film is a tetragonal perovskite structure. The XRD spectra of the $CH_3NH_3Pb(SCN)_xI_{3-x}$ perovskite films ($x > 0$) showed an additional peak at 12.66° and its intensity increased with SCN concentration. The carbon-based hole-transport-layer (HTL) free $CH_3NH_3Pb(SCN)_xI_{3-x}$ (at $x = 0.0625$) perovskite solar cell had the optimal SCN^- dopant ratio, generating a promising cell efficiency of 6.34%, with a good efficiency retention of 79.43% after 30 days of testing, in comparison to a pure $CH_3NH_3PbI_3$ perovskite solar cell with an efficiency retention of only 26.92%.

Keyword : perovskite, solar cell, CH3NH3PbI3

ACKNOWLEDGEMENTS

This work was supported by the Research Network NANOTEC (RNN) program of the National Nanotechnology Center (NANOTEC), NSTDA, Ministry of Higher Education, Science, Research, and Innovation (MHESI) and Khon Kaen University, Thailand, The institute for the Promotion of Teaching Science and Technology (IPST), Thailand, and by Thailand Science Research and Innovation and Srinakharinwirot University (Contract No. 028/2564), and by the Thailand Center of Excellence in Physics (ThEP).

PRIMPRAPHA PRASAN

TABLE OF CONTENTS

Page

LIST OF TABLES

Page

LIST OF FIGURES

Page

CHAPTER 1
INTRODUCTION

Background

In 21st century, energy is one of the most essential sources for mankind activities including the economy, traffic, technology or even the environmental pollution. The energy demand persistently increases due to the continuous growth of the world's population especially in the metropolitan areas, while gas and oil rapidly decrease in a short time. Therefore, the renewable energy has attracted much attention due to its clean and long-term energy. Solar energy has been known as the most innumerable of all-natural energy resources, which can provide energy for more than billions of years and can be harvested in all the sunlight areas. Interestingly, the solar energy that come from sunlight impacted on the Earth's surface, is approximately 1 x 10^5 tetra watt per day. This amount of solar energy can provide the required electric energy for all year. Solar cell was invented to convert the solar energy to electric energy referred as Photovoltaic effect. However, the manufacturing cost is considerably higher than those of natural gas and oil. This drawback factor limits the large personal uses.

The first silicon solar cell was informed in 1954 by Chappin, Fuller and Pearson. The device transformed sunlight into electricity by the P-N junction silicon solar cell with an efficiency of 6%. During 1950s and 60s, the silicon solar cells were applied in the space application. However, the silicon solar cell had not obtained much attendance from researchers, scientists and entrepreneurs due to the expensive manufacturing cost and sophisticated production. Subsequently, the alternative materials such as polycrystalline silicon, amorphous silicon, thin film materials and organic conductors were used for manufacturing the lower cost of solar cell. Nonetheless, none of these materials induced the extensive commercialization of the solar cells. (Jenny Nelson, 2003)

In 1991, Micheal Gratzel reported the new type of solar cell called " Dye-sensitized solar cell (DSSC) or Gratzel's cell". (O'Regan & Grätzel, 1991) The solar cell had immensely attracted attentions from scientists, researchers and entrepreneurs all over the world because of its low-cost and great cell's efficiency. Onwards, The

$CH_3NH_3PbI_3$ Perovskite materials was first reported in 2009, which was successfully substituted the dye pigment in the absorption layer of Dye-sensitized solar cells (DSSCs). This discovery lead to the development of the new solar cell called " Perovskite solar cell". (สมัคร์, 2556)

The organic-inorganic halide perovskite solar cells have attracted much attention from research community and considered to be the promising photovoltaic candidate as a future renewable energy resource. This is because of its low cost and rapid growth of efficiency from 3.8% in 2009 to 25% after a decade. (T. Kim, Lim, & Song, 2020) The organic-inorganic halide perovskite material has the general formula ABX_3, where A is an organic cation ($CH_3NH_3^+$ or $NH_2CH_3NH_2^+$), B is a divalent cation ($Pb2^+$ or $Sn2^+$) and X is a monovalent halide anion (I^-, Br^- or Cl^-). The perovskite materials have been represented with greatly adjustable bad gap (e.g., $CH_3NH_3PbX_3$ has energy band gap from 1.5 eV to 2.3 eV) and excellent light absorption coefficient (higher than 10^4 cm^{-1}) (Shi & Jayatissa, 2018) The perovskite solar cells have been developed from the mesoscopic structure, which the perovskite layer displaced the light harvesting dye pigment. The evolution of the perovskite solar cell's structures is represented in 4 different features as seen in Figure 1(a-d). The n-i-p structure is called ordinary device structure and p-i-n structure is called converted device structure. The structures are defined by the position of electron transport materials (ETM) and hole transport materials (HTM). (Elumalai, Mahmud, Wang, & Uddin, 2016)

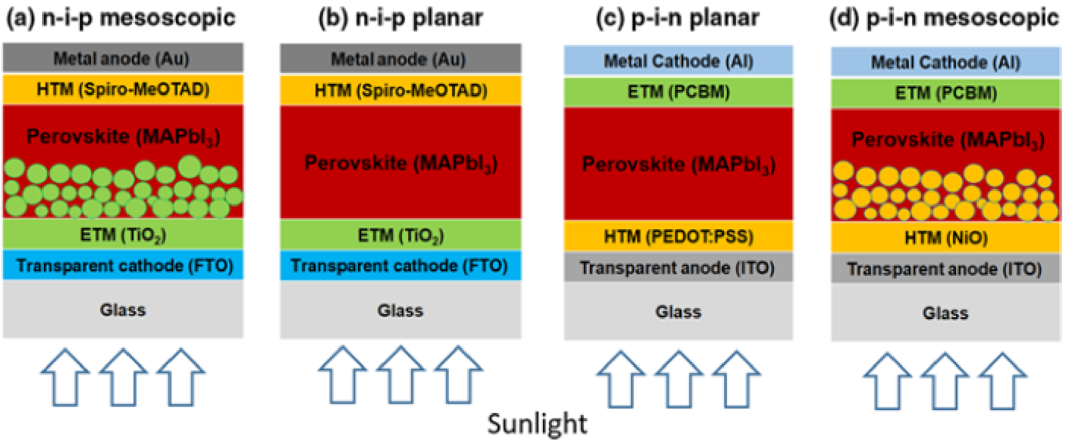

Figure 1 Schematic diagrams of perovskite solar cells in the (a) n-i-p mesoscopic, (b) n-i-p planar, (c) p-i-n planar and (d) p-i-n mesoscopic structures.

Source: Elumalai NK, Mahmud MA, Wang D, Uddin A. Perovskite Solar Cells: Progress and Advancements. Energies. 2016;9:861.

However, the poor stability of the organic-inorganic halide perovskite solar cells in ambient air has restricted the large-scale commercialization. To solve this problem, Tai et al. reported the application of Lead (II) Thiocyanate ($Pb(SCN)_2$) precursor in preparing perovskite solar cells under ambient environment. They found that $CH_3NH_3PbI_{3-x}(SCN)_x$ perovskite films exhibited the great efficiency of 13.49% and considerably maintained 86.7% of the initial average efficiency after testing in relative humidity over 70% for 500 hours. In comparison, the pure $CH_3NH_3PbI_3$-based perovskite solar cells remained 40% of the initial PCE, the $CH_3NH_3PbI_{3-x}(SCN)_x$ solar cells. This demonstrates that the $CH_3NH_3PbI_{3-x}(SCN)_x$ perovskite film is better stability in humid atmosphere than that the pure $CH_3NH_3PbI_3$ film as shown in Figure 2. (Tai et al., 2016)

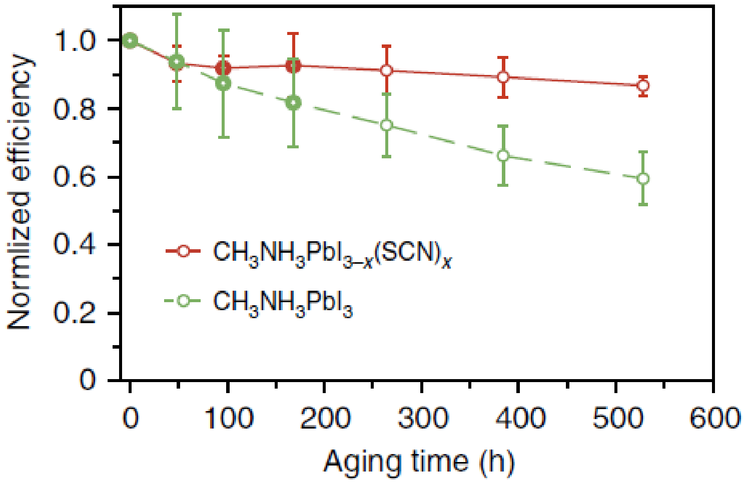

Figure 2 Evolution of the PCEs of CH3NH3PbI3-x(SCN)x- and CH3NH3PbI3-based solar cells upon ageing in air without encapsulation.

Source: Tai Q, You P, Sang H, Liu Z, Hu C, Chan HLW, et al. Efficient and stable perovskite solar cells prepared in ambient air irrespective of the humidity. Nature Communications. 2016;7(1):11105.

M. K. Kim et al. studied the addition of Lead (II) Thiocyanate ($Pb(SCN)_2$) in $CH_3NH_3PbI_3$ with 6 different concentrations (0, 0.1, 0.12, 0.15 and 0.18 mol). They found that the addition of 0.3 mol $Pb(SCN)_2$ concentration in $CH_3NH_3PbI_3$ increases PCE to 11.6%, which is 90% higher than that of the pure $CH_3NH_3PbI_3$ perovskite solar cells (6.08%). Furthermore, the addition of $Pb(SCN)_2$ induces the grain-size enlargement approximately from 150 nm to 5 μm as seen in Figure 3(a-f), which induces the extension of carrier lifetime and reduces the hysteresis effect. (M. K. Kim et al., 2016)

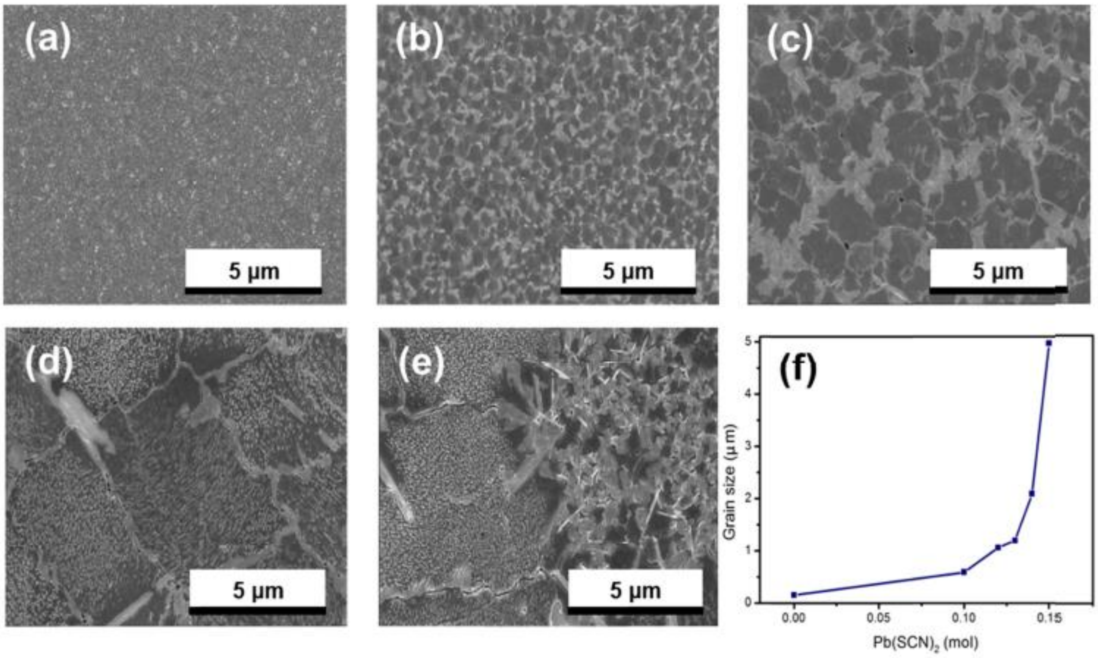

Figure 3 (a) – (e) Plane view SEM images of perovskite films with different amounts of $Pb(SCN)_2$ additive (a) 0 mol, (b) 0.1 mol, (c) 0.12 mol, (d) 0.15 mol and (e) 0.18 mol. (f) a plot of grain size vs. $Pb(SCN)_2$ amount.

Source: Kim MK, Jeon T, Park HI, Lee JM, Nam SA, Kim SO. Effective control of crystal grain size in CH3NH3PbI3 perovskite solar cells with a pseudohalide Pb(SCN)2 additive. CrystEngComm. 2016;18(32):6090-5.

Ke et al. prepared $CH_3NH_3PbI_{3-x}(SCN)_x$ perovskite films by adding $Pb(SCN)_2$ into $CH_3NH_3PbI_3$ with 4 different percentages (2.5%, 5.0%, 7.5% and 10.0%) via one-step deposition. The addition of $Pb(SCN)_2$ into $CH_3NH_3PbI_3$ significantly enlarges the perovskite grain size. The films' surfaces are smooth and continuous and the films' thicknesses are quite the same as the pure $CH_3NH_3PbI_3$ film as represented in Figure 4(a-d). The perovskite solar cell with 5% of $Pb(SCN)_2$ addition had notably reduced the hysteresis and greatly increased the efficiency to 18.53% in comparing to the pure $CH_3NH_3PbI_3$ perovskite solar cell (15.57%). (Ke et al., 2016)

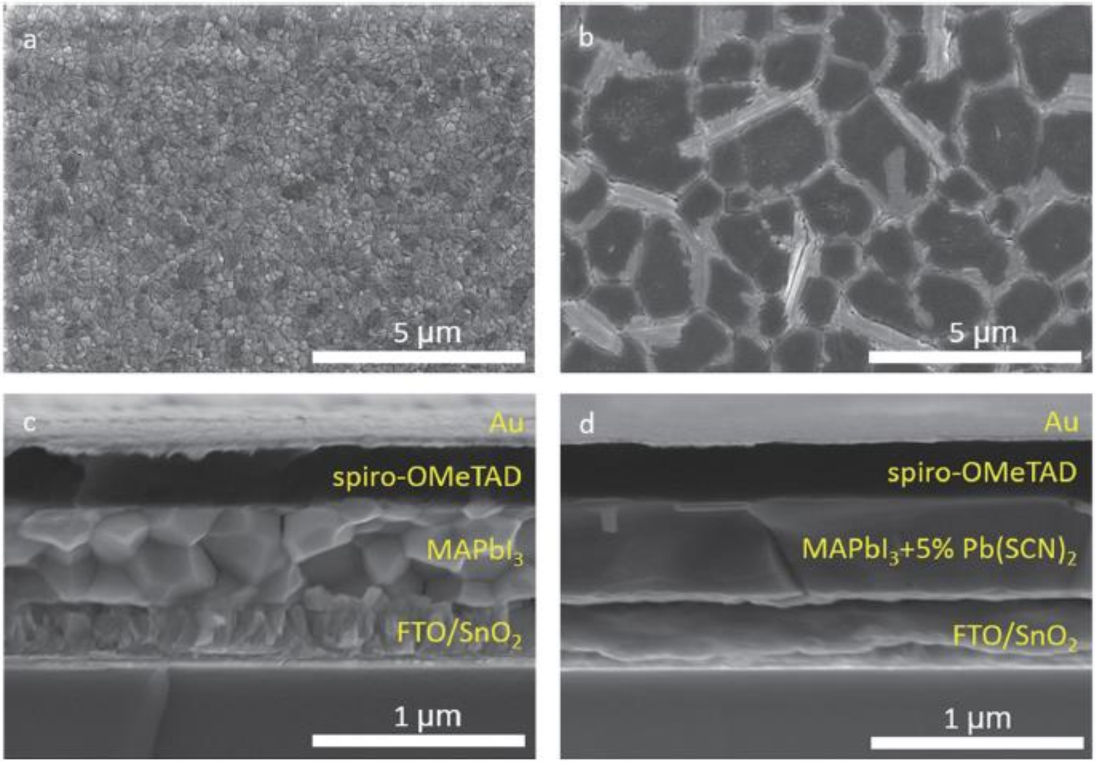

Figure 4 (a), (b) Top-view images of $CH_3NH_3PbI_3$ film (a) without $Pb(SCN)_2$ and (b) with 5% of $Pb(SCN)_2$ in the precursor. (c), (d) Cross-sectional SEM images of completing devices using $CH_3NH_3PbI_3$ (c) without $Pb(SCN)_2$ and (d) with 5% of $Pb(SCN)_2$ in the precursor.

Source: Ke W, Xiao C, Wang C, Saparov B, Duan H-S, Zhao D, et al. Employing Lead Thiocyanate Additive to Reduce the Hysteresis and Boost the Fill Factor of Planar Perovskite Solar Cells. Advanced Materials. 2016;28(26):5214-21.

Through the literature reviews, the $CH_3NH_3Pb(SCN)_xI_{3-x}$ perovskite exhibits the better efficiency and stability than that of the pure $CH_3NH_3PbI_3$ perovskite. It can be prepared under humid environment and they are also suitable for the light harvester because the energy gap of $CH_3NH_3Pb(SCN)_xI_{3-x}$ are quite similar to the energy gap of the pure $CH_3NH_3PbI_3$ film. Therefore, This research aims to study the effects of the $CH_3NH_3Pb(SCN)_xI_{3-x}$ films at x = 0, 0.0625, 0.125, 0.1875, 0.25 and 0.5 on the film's morphology, crystallite and energy gap. The efficiency and stability of the $CH_3NH_3Pb(SCN)_xI_{3-x}$ perovskite solar cells were tested and analyzed in detail. The $CH_3NH_3Pb(SCN)_xI_{3-x}$ films at x = 0, 0.0625, 0.125, 0.1875, 0.25 and 0.5 will be prepared by one-step hot casting method. The film's morphology, crystal structure and light absorption were analyzed by using Scanning Electron Microscope (SEM), X-Ray diffraction (XRD) and UV-Vis spectroscopy, respectively for explain the variation of the cell efficiency and stability.

Objectives of the Study

1. Synthesize $CH_3NH_3Pb(SCN)_xI_{3-x}$ films at x = 0, 0.0625, 0.125, 0.1875, 0.25 and 0.5 using $Pb(SCN)_2$, PbI_2 and CH_3NH_3I precursors on the TiO_2 layer.
2. Investigate the effect of SCN^- moiety on the $CH_3NH_3Pb(SCN)_xI_{3-x}$ film's morphology, crystallite and absorption coefficient.
3. Invent carbon-based hole-transport-layer-free perovskite solar cell using $CH_3NH_3Pb(SCN)_xI_{3-x}$ films at x = 0, 0.0625, 0.125, 0.1875, 0.25 and 0.5 as the absorption layer, and test the solar cell's efficiency and stability.

Significance of the Study

1. Obtain the $CH_3NH_3Pb(SCN)_xI_{3-x}$ films at x = 0, 0.0625, 0.125, 0.1875, 0.25 and 0.5 by one-step hot-casting method.
2. Understand the effect of SCN^- moieties on the $CH_3NH_3Pb(SCN)_xI_{3-x}$ film's morphology, crystal structure and light absorbing properties.
3. Obtain the carbon-based hole-transport-layer-free $CH_3NH_3Pb(SCN)_xI_{3-x}$ perovskite with power conversion efficiency (PCE) over 7% and the efficiency retention of 80% after 30 days.

Scope of the Study

1. Synthesis $CH_3NH_3Pb(SCN)_xI_{3-x}$ films at x = 0, 0.0625, 0.125, 0.1875, 0.25 and 0.5 using $Pb(SCN)_2$, PbI_2 and CH_3NH_3I precursors on TiO_2 layer by one-step hot-casting method.

2. Analyze the effect of SCN^- moiety on the $CH_3NH_3Pb(SCN)_xI_{3-x}$ films at x = 0, 0.0625, 0.125, 0.1875, 0.25 and 0.5 on the morphology, crystallite and absorption.

3. Assemble and test the efficiency and stability of the the carbon-based hole-transport-layer-free perovskite solar cells.

CHAPTER 2
LITERATURE REVIEW

In this research, we had studied and assembled the carbon-based perovskite solar cells, which is related to the thesis topic of "EFFICIENCY OF $CH_3NH_3Pb(SCN)_xI_{3-x}$ FILMS AS LIGHT ABSORBER IN CARBON-BASED HOLE-TRANSPORT-LAYER-FREE PEROVSKITE SOLAR CELLS". The literature review chapter will be presented as the following.

1. The theory of solar cell.
2. The theory of perovskite solar cell.
3. Working principle of the analyzing equipment.
4. Related papers.

1. The theory of solar cell

A solar cell is defined as an electrical device that directly converts the light energy into the electrical energy by the photovoltaic effect. Solar cells provide the electrical characteristics such as voltage, current or resistance varying under light illumination.

1.1. The structure of solar cells

A solar cell is basically a sandwich of P-type semiconductor layer and N-type semiconductor layer, which is similar to a diode. However, the structure of a solar cell is slightly different from a conventional P-N junction diode which consists of front electrode, a layer of N-type semiconductor, a layer of P-type semiconductor and back electrode as seen in Figure 5. Thus, a solar cell can be defined as a battery is parallel with a diode.

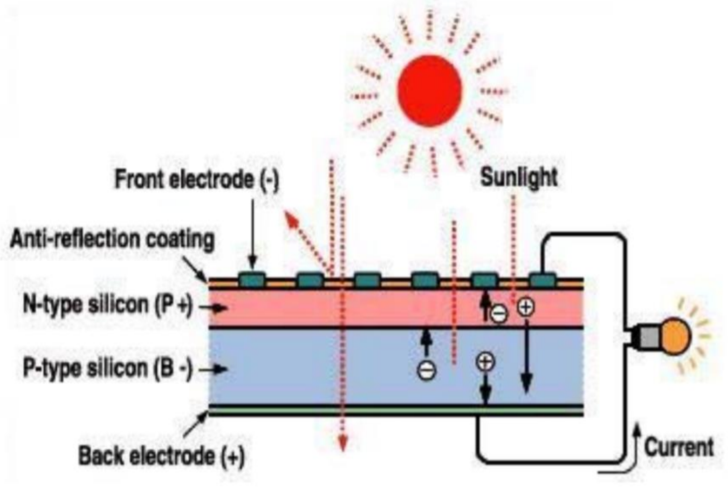

Figure 5 The schematic of a solar cell structure.

Source: Su, Q., Zhang, G., Lai, J., Feng, S., & Shi, W. (2011). Green Solar Electric Vehicle Changing the Future Lifestyle of Human. World Electric Vehicle Journal, 4, 128-132. doi:10.3390/wevj4010128

1.2. Working principle of solar cells

Solar cell can generate electricity when the light energy in term of photons entered the P-N junction with a sufficient energy. The photons can easily create a number of electron-hole pairs (exciton). Afterwards, the free-electrons will actively move to the N-type layer and the holes will move to the P-type side. This phenomenon will continuously repeat under the light illumination. Eventually, the concentration of electrons and holes increases, the device will behave as a small battery and generate photovoltage. If a load is connected across the junction, there will have a current flowing through the load. The entire current, which is directly generated from the solar cell, is called “Short circuit current density: J_{sc}”. When the load is disconnected to the circuit, the different electrical potential increases between terminals. The potential difference induces a current, which flows through the diode, called “J_D”. (Jenny Nelson, 2003) The photocurrent is separated into the diode and the resistance. The net current flowing through the load depends on the resistance of the load and the concentration of illumination as seen in Figure 6. (สมัคร์, 2556)

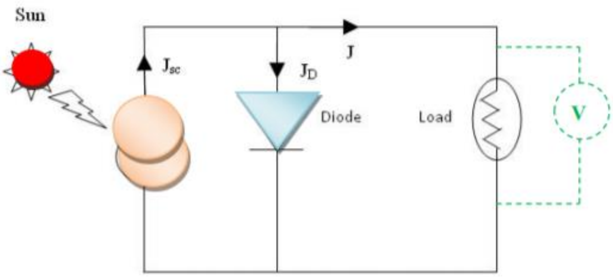

Figure 6 The schematic of an ideal solar cell.

Source: สมัคร์, พ. (2556). *ทฤษฎีเซลล์แสงอาทิตย์เบื้องต้น*. ขอนแก่น: ภาควิชาฟิสิกส์, มหาวิทยาลัยขอนแก่น.

The net current density (J) can be defined as equation (2.1)

$$J = J_{sc} - J_D \tag{2.1}$$

The diode current density (J_D) varies as the following equation

$$J_D = J_0\left(e^{\frac{qV}{k_B T}} - 1\right) \tag{2.2}$$

Where, J_0 is a constant
q is an electric charge (1.6 x 10^{-19} C)
V is potential difference of the cells
k_B is Boltzmann's constant
T is temperature (K)

Thus, the equation of the net current density for the ideal solar cell is

$$J = J_{sc} - J_0\left(e^{\frac{qV}{k_B T}} - 1\right) \tag{2.3}$$

The constant light illumination source could induce the stable short circuit current density (J_{sc}). From the equation (2.3), the net current density will have specific characteristic under light illumination (Light, $J_{sc} \neq 0$) and in the dark (Dark, $J_{sc} = 0$) as seen in Figure 7. (Jenny Nelson, 2003)

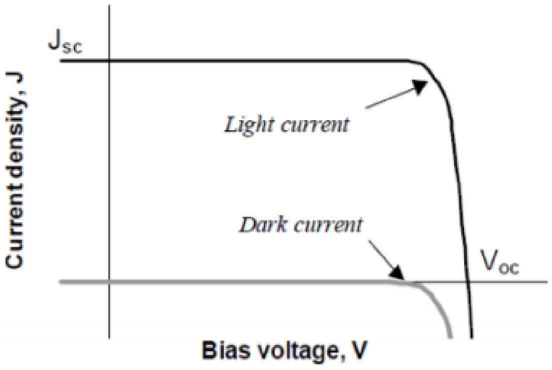

Figure 7 the current density will be approximated under light illumination (Light, $J_{sc} \neq 0$) and in the dark (Dark, $J_{sc} = 0$)

Source: Jenny Nelson. (2003). *The Physics of Solar Cells*. London: Imperial College Press.

From Figure 7, the dark current curve represents a familiar diode characteristic. The difference between the light current curve and a typical diode curve is that the y-axis of the light current curve is the superposition of a diode curve in the first quadrant. The superposition is based on the intensity of the light, which shines on the solar cell surface.

1.3 Important parameters of solar cells

Solar cell is known as an electrical device, which supplies the electrical power. To estimate the performance of the solar cell, the important parameters will be evaluated using a solar simulator and the photocurrent (J) versus photvoltage (V) curves are obtained as seen in Figure 8.

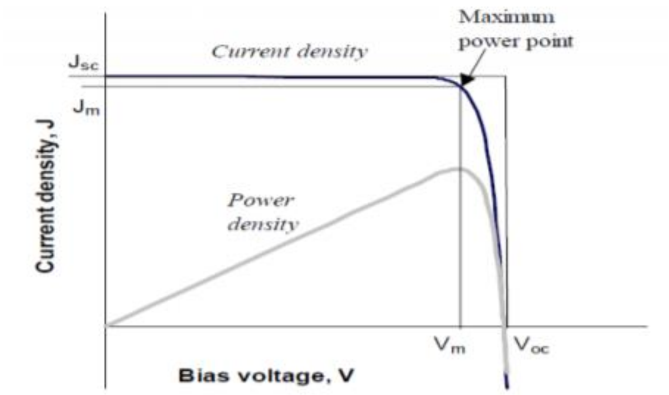

Figure 8 The J-V curve of an ideal solar cell.

Source: Jenny Nelson. (2003). The Physics of Solar Cells. London: Imperial College Press.

1.3.1 Short circuit current density (J_{sc}) and Open-circuit voltage (V_{oc})

The represented black line in Figure 8 is called J-V curve. The intersection on y-axis of the J-V curve demonstrates the short circuit current density (J_{sc}), and the intersection on x-axis of the J-V curve shows open-circuit voltage (V_{oc}). The short circuit current density (J_{sc}) is obtained when the zero-resistance load or near zero resistance load is affixed to the device. Thus, the short circuit current density is the highest current density with the zero voltage, and J_{sc} varies linearly with the light intensity. The open-circuit voltage (V_{oc}) is obtained at the high resistance load or infinite- resistance load is attached to the solar cell. Therefore, the open-circuit voltage (V_{oc}) is the highest voltage at the zero-current, and V_{oc} varies logarithmically to the light intensity.

1.3.2 Maximum power point ($P_{\max}$)

The J-V curve is presented in two axes, which are the current density (J) on the y-axis and the voltage (V) on the x-axis. The product of the two axes is the power density (P), the device power density is given by

$$P = JV \qquad (2.4)$$

The power density at a maximum point is called the maximum power point ($P_{\max}$). This initiates the maximum voltage (V_m) and the maximum current density (J_m) as seen in Figure 8. The maximum power point ($P_{\max}$) is the most interesting value because the maximum power point is the authentic power, which delivers from a solar cell under the given conditions. (Jenny Nelson, 2003)

1.3.3 Fill factor (FF)

Fill factor (FF) is one of the essential solar cell parameters because fill factor indicates the idealism of a solar cell and describes the squareness of the J-V curve. Fill factor (FF) is defined as the ratio

$$FF = \frac{J_m V_m}{J_{sc} V_{oc}} \qquad (2.5)$$

Fill factor depends on the internal resistance of the device.

1.3.4 Efficiency (η)

The efficiency (η) of a solar cell is the ratio of the power maximum power point ($P_{\max}$) and the incident light power density (P_{in})as the following equation

$$\eta = \frac{P_{\max}}{P_{in}} = \frac{J_m V_m}{P_{in}} \qquad (2.6)$$

$$\eta = \frac{J_{sc} V_{oc} FF}{P_{in}} \qquad (2.7)$$

It sees that the efficiency of the device is related to J_{sc}, V_{oc} and FF. These four parameters: J_{sc}, V_{oc}, FF and η are the key performance characteristics of a solar cell under the particular illumination conditions. (Jenny Nelson, 2003)

1.3.5 Parasitic resistances

In realistic, the power of solar cell is also dispersed through the resistance of the contacts and the leakage currents around the junction of the device. These effects are impartial electrically to the series resistance (R_s) and the shunt resistance (R_{sh}) in the cell (สมัคร์, 2556) as seen in Figure 9.

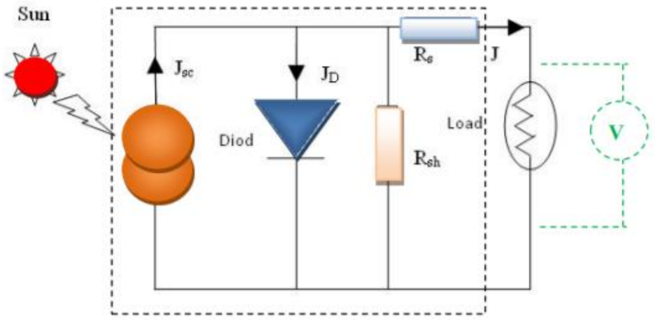

Figure 9 Equivalent circuit including series resistance (R_s) and shunt resistance (R_{sh}).

Source: สมัคร์, พ. (2556). *ทฤษฎีเซลล์แสงอาทิตย์เบื้องต้น*. ขอนแก่น: ภาควิชาฟิสิกส์, มหาวิทยาลัยขอนแก่น.

The series resistance occurs from the material resistance and the contact between conductor and materials. The parallel or shunt resistance emerged from the leaking current through the p-n junction. The low shunt resistance will cause the poor device performance. (Jenny Nelson, 2003)

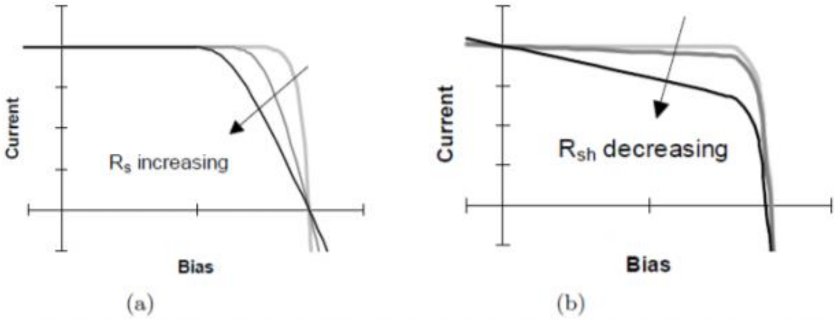

(a) (b)

Figure 10 Effect of (a) increasing series resistance and (b) reducing parallel resistance.

Source: Jenny Nelson. (2003). The Physics of Solar Cells. London: Imperial College Press.

Series and shunt resistances reduce the fill factor as shown in Figure 10. For the high solar cell efficiency, the series resistance should be small but the shunt resistance should be large.

2. The theory of perovskite solar cells

2.1 Perovskite crystal structure

The crystal structure of perovskite compounds is generally ABX_3, where A and B are the +1 and +2 charged cations, respectively, and X atom is the -1 charged anion. From Figure 11, atom A is larger than atom B, where atom A is chosen in order to balance the crystal structure with all charges, and atom A may be a substance derived from hydrocarbons, for instance methyl ammonium ions. (methylammonium: $CH_3NH_3^+$), ethyl ammonium ion (ethyl ammonium: $CH_3CH_2NH_3^+$), formidinium ion (formamidinium: $NH_2CH{=}NH_2^+$) or derived from metals such as cesium ion (Cesium: Cs+). B is a metal cation (metal cation), such as germanium ion (Germanium: Ge^{2+}), tin (II) ion (Tin: Sn^{2+}), Lead (II) ion (Lead: Pb^{2+}). X atom is the negative ion such as F^-, Br^-, I^- and Cl^-. (Di Giacomo, Fakharuddin, Jose, & Brown, 2016)

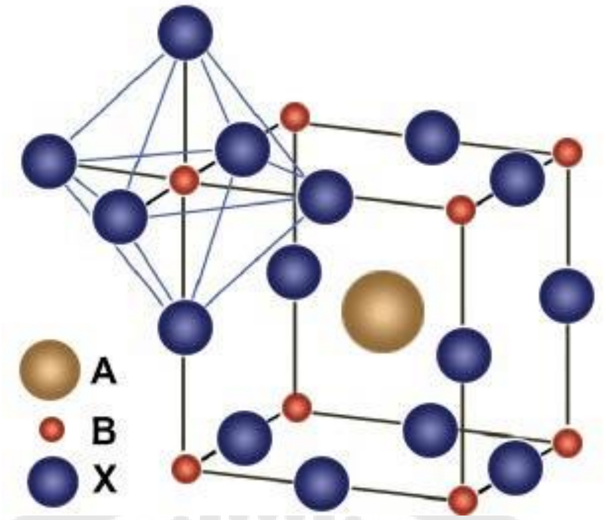

Figure 11 Perovskite crystal structure.

Source: Di Giacomo, F., Fakharuddin, A., Jose, R., & Brown, T. M. (2016). Progress, challenges and perspectives in flexible perovskite solar cells. Energy & Environmental Science, 9(10), 3007-3035. doi:10.1039/C6EE01137C

Methyl ammonium iodide compound (Methylammonium lead iodide: $MAPbI_3$) is a perovskite, which has been widely used as an absorbent layer in perovskite photovoltaic systems. Nevertheless, many researchers have attempted to replace the $MAPbI_3$ compound by substituting thiocyanate (SCN^-) ions, which is a pseudo-halide with similar properties to the halide ions. The SCN^- moiety has the ion radius about 0.215 - 0.22 nm, and I^- moiety has an ion radius of 0.22 nm. (Chen, Li, Huang, Gao, & Liang, 2015; Lou et al., 2018; Tai et al., 2016) Interestingly, doping a small amount of SCN^- into $MAPbI_3$ results in better light absorption, greater charge transportation and higher current density. Importantly, the formation of $MAPbI_{3-x}(SCN)_x$ perovskite film has a large crystal size, which reduces electron and hole recombination. (Tai et al., 2016)

2.2 The structure of perovskite solar cell

Perovskite solar cells have three main components: the part of working electrode, hole-transport-materials and counter electrode as seen in Figure 12.

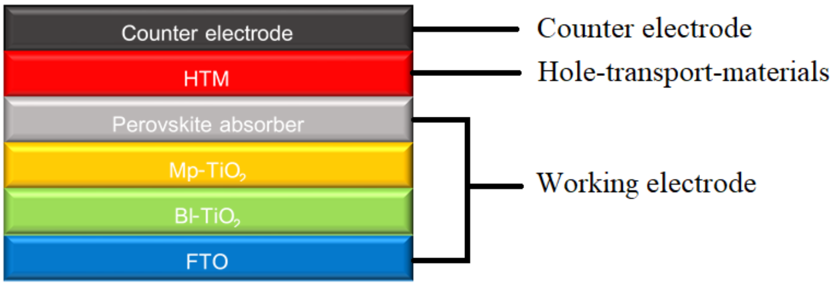

Figure 12 The structure of perovskite solar cell.

2.2.1 Working electrode

The working electrode consist of several important subsections such as the transparent conducting material (FTO), the blocking-TiO_2 layer or compact TiO_2 layer (bl- TiO_2), the mesoporous TiO_2 layer (mp - TiO_2) and the absorbing layer or perovskite layer. Each layer has different functions as described in the following lists.

1) Substrate material of the solar cell

The transparent conductive oxide glass (TCO) is normally used for the substrate of perovskite solar cell (PSC). There are two types of the conductive glass which are applied in the solar cell manufacturing such as Fluorine doped Tin Oxide (FTO) and Indium doped Tin Oxide (ITO). The FTO glass has attracted more attention from the researchers due to the better heat resistance than that of ITO glass, and the less reduction of electrical conductivity at high temperature

2) blocking-TiO_2 layer or compact TiO_2 layer (bl- TiO_2)

The blocking TiO_2 layer obstructs the retrace of excited electrons from the conductive glass to the perovskite layer and prevents short circuit of solar cells.

3) mesoporous TiO_2 layer (mp - TiO_2)

The mp- TiO_2 layer acts as an electron-transmitting layer between the absorption perovskite layer and FTO, and it also hinders the recombination between electrons in the conductive glass layer and holes at the back electrode (carbon). The mp-TiO_2 layer increases the contact area between the perovskite layer and the titanium oxide film.

4) Perovskite absorption layer

The perovskite layer absorbs sunlight to excite electron at ground state to the excited state. This creates the electron-hole pair (exciton) into the cell, afterwards electrons will be delivered to the electron-transport-layer and hole will be injected to the hole-transport-layer.

2.2.2 Hole-transport-material (HTM)

Hole-transport-material is a solid material that performs as P-type semiconductor, which has two types: organic and inorganic. The examples of widely used organic hole-transport-materials are spiro-OMeTAD, P3HT, PCPDTBT, PCDTBT or PTAA, and the examples of the inorganic materials are CuI, CuSCN and $CsSnI_3$. These hole-transport-materials are responsible for the hole transmission from the valence band (VB) of perovskite layer to the counter terminal.

2.2.3 Counter electrode

Generally, perovskite solar cell assembly using gold (Au) and silver (Ag) metals as counter electrodes. Holes from perovskite layer will be injected to the back conducting metal, and exported to the external circuit. In this research, carbon films will be used as the counter electrode due to its low-cost material and facile fabrication.

2.3 Preparation process of perovskite film

Perovskite film is generally synthesized from the reaction between lead halide salt and methylammonium salt (MAI) according to the following equation

$$CH_3NH_3I + PbI_2 \rightarrow CH_3NH_3PbI_3 \tag{2.8}$$

There are two main methods to prepare and control the perovskite reaction: 1) Single-step or one-step deposition and 2) double-step or two-step deposition. One-step deposition method, the precursors are dissolved in solvent together, but two-step deposition method, the precursors are dissolved in separate solvent. However, the sub-processes such as spin-coating, vapor-assisted vacuum deposition, hot-casting or thermal evaporation deposition could be performed in the fabrication of solar cells. (Di Giacomo et al., 2016) In this research, the perovskite film will be synthesized using one-step spin-coating method together with a hot-casting method, which will be described in detail in the following topic.

2.3.1 One-step or single-step spin coating

In one-step coating, CH_3NH_3I and PbI_2 were dissolved together in the same solution. The solvents used to dissolve the precursors mostly are N,N-Dimethylformamind anhydrous (DMF), Dimethyl sulfoxide anhydrous (DMSO) or ɤ -Butyrolactone (GBL) for the solvents. (Di Giacomo et al., 2016) Afterward, the solution will be deposited on the substrate using spin-coating method, and films were annealed at 100°C for 10 minutes to form the perovskite film. The heat will quickly evaporate solvents from the film. This method directly induces the perovskite film formed on the substrate (FTO). In order to obtain a continuous and smooth perovskite film on the substrate surface, the crystallization is very important and has to be cautiously controlled during the processing.

2.3.2 Hot-casting method

Hot-casting is the process of heating a substrate first before spinning the solution. The TiO_2 layer (FTO/bl- TiO_2/mp- TiO_2) is heated to a high temperature 145°C before quickly spin coating the solution on the substrate. This hot-casting method results in the large grain and continuous film surfaces.

2.4 Working principle of perovskite solar cell

The working principle of perovskite solar cell can be divided into 4 steps as detailing below.

Step 1: The perovskite layer collects energy from sunlight, the excitons will be occurred and separate to free-electrons and free-holes.

Step 2: The electrons in the excitation state automatically transport to the conduction band of the metal oxide semiconductor (TiO_2), and then they are injected the conductive glass (FTO).

Step 3: The holes move to the hole-transport-material (HTM) and is forwarded to the counter electrode.

Step 4: The electron and hole flow into the external circuit (electrical load) resulting in the electrical current flowing through the external device.

If there is a continuous incident of solar energy on the solar cell, these four processes will continuously occur. The working principle of perovskite solar cell in all 4 steps are summarized as shown in Figure 13. (พรรณธิวา, 2562)

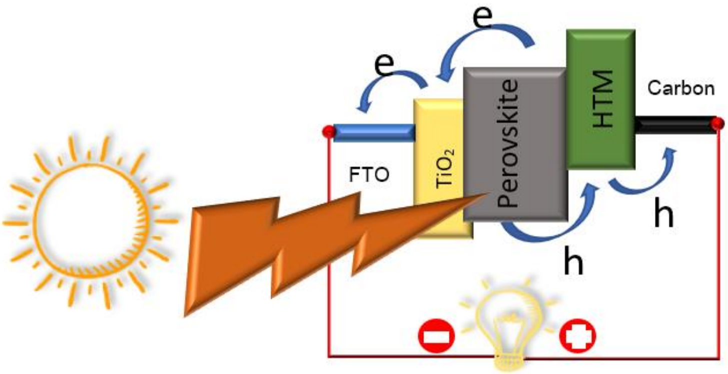

Figure 13 Working principle of perovskite solar cell.

3. Working principle of the measuring equipment

3.1 Characterizing $CH_3NH_3Pb(SCN)_xI_{3-x}$ thin film

In this work, the properties of $CH_3NH_3Pb(SCN)_xI_{3-x}$ thin film at x = 0, 0.0625, 0.125, 0.1875, 0.25 and 0.5 will be analyzed as follows. 1) The film morphology will be analyzed using Scanning Electron Microscope (SEM). 2) The optical properties of the perovskite film will be by UV-VIS spectroscopy. 3) The crystal structure will be studied using X-Ray diffraction technique (XRD). 4) The elemental percentages will be analyzed using Energy Dispersive X-ray spectroscopy (EDX) technique. The working principles of these analyzers will be described in the following.

3.1.1 Scanning Electron Microscope (SEM)

Scanning electron microscope (SEM) is a type of electron microscope that photographs a specimen by emitting high-energy electrons from a source (electron gun), which are accelerated by an electric field onto a condenser lens. The condenser lens combines electrons into a smaller electron beam. Afterward, the electron beam passes through the objective lens. The objective lens will focus the electron beam on the sample surface. The scan coil acts to scatter electron beams on the surface of the sample in a small rectangular area. This causes various signals such as back scattered electron, secondary electron, X-Ray, Auger electron and electromagnetic wave. The images of perovskite film will be obtained from the secondary electron signal. (ดนัย กิจชัยนุกูล, 2547) The components of the scanning electron microscopy (SEM) instrument are shown in Figure 14.

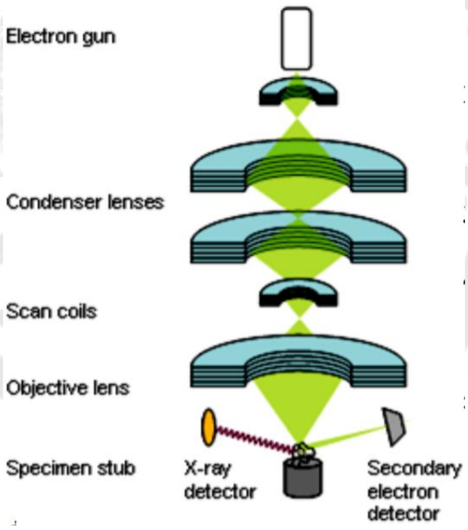

Figure 14 The components of the scanning electron microscopy (SEM)

Source: จักรพันธ์ ถาวรธิดา. (2020). *กล้องจุลทรรศน์อิเล็กตรอน Electron microscope*. ชลบุรี: คณะวิทยาศาสตร์ มหาวิทยาลัยบูรพา.

3.1.2 UV-Vis spectroscopy

Figure 15 UV-VIS spectroscopy

Source: science, N. m. I. UV-1800 UV-VIS Spectrophotometer. https://www.news-medical.net/UV-1800-UV-VIS-Spectrophotometer-from-Shimadzu

UV-Vis spectroscopy is a technique used to measure the amount of light absorbance of a sample, which is in the range ultra violet to visible light (190-800 nm). The absorbance properties of substances can be used for both qualitative and quantitative analysis because this method has the good accuracy and high sensitivity. There are two components of a UV-vis spectroscopy: an ultraviolet light source and a visible light source. Working principle of UV-vis spectroscopy is shown in Figure 16, and clarified in the next paragraph.

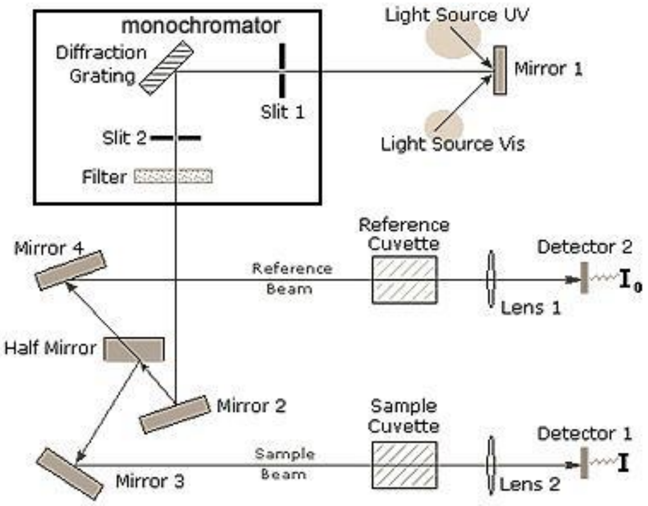

Figure 16 Working principle of UV-VIS spectroscopy.

Source: Sun, J. (2014). Development of Inorganic-Organic Hybrid Materials for Waste Water Treatment. Retrieved from https://www.researchgate.net/figure/A-dual-beam-UV-vis-spectrophotometer-8_fig20_314081363

First of all, the light from both sources strikes mirror 1 (mirror 1), then passes through slit 1 and reaches the diffraction grating. The grating can be rotated to select a specific wavelength, then the selected wavelength beam passes through slit 2 and a light filter which will filter the disruptive light and the uplifting light intensity out of the beam. After that, the beam hits on the second mirror (mirror 2), then the beam is directed to the half mirror, which divides the light into two parts equally. The half of the beam will be sent to the cuvette of the sample and the other half will be reflected to the reference cuvette. (พรรณธิวา, 2562)

3.1.3 X-Ray diffraction (XRD)

Figure 17 X-Ray diffraction (XRD)

Source: Management, D. PANalytical Empyrean – เครื่องวัดการเลี้ยวเบนของรังสีเอ็กซเรย์ (XRD). https://www.dksh.com/th-th/products/ins/panalytical-empyrean

X-ray diffraction analysis is a technique used to study the crystal structure of a sample based on the principle of X-ray diffraction. When a X-ray beam hits an object or the particle will be refracted. The reflected ray has an angle equal to the incidence beam angle according to the Bragg's law as shown in the equation 2.9. X-ray diffraction data obtained from the instrument will be compared with the standard data from Joint committee on powder diffraction standards (JCPDs) to identify the type of crystal structure and crystal plane.

$$2d \sin\theta = n\lambda \qquad (2.9)$$

Where d is the spacing of the crystal layers (path difference),

λ is the wavelength of the x-ray,

θ is the incident angle (the angle between incident ray and the scatter plane) and,

n is an integer.

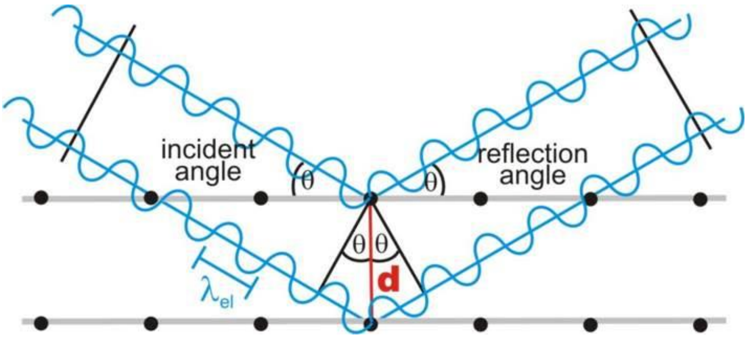

Figure 18 Constructive Interference of reflected waves

Source: Krumeich, F. (2020). Bragg's Law of Diffraction. Retrieved from https://www.microscopy.ethz.ch/krumeich.htm

3.1.4 Energy dispersive X-ray spectroscopy (EDX)

Figure 19 Mini Scanning electron microscope (SEM, sec, sne-4500m)

Source: nano, A. SNE-4500M Tabletop SEM with 5-Axis Stage Control. https://www.azonano.com/equipment-details.aspx?EquipID=1470

Energy dispersive X-ray spectroscopy (EDX) is an equipment that used to analyze elements on samples. It can analyze various elements from carbon to uranium. This technique is widely used because it is the convenience and it can be analyzed in all condition including solid, liquid or powder samples.

The principle of this technique is that the X-rays from the source eject the outermost electrons of the element's atoms. Next, the higher energy electron will drop to replace the lost electrons, and emit energy out in the form of x-ray. The specific energy value is obtained from each element. (ธิติ มหาเจริญ, 2561)

3.2 The solar simulator

The efficiency of the prepared perovskite solar cells in this research will be tested using the commercial solar simulator. The standard light intensity value used in testing solar cell efficiency test is 100 mW/cm^2 under AM 1.5 standard light (1.5 Atmosphere mass).

Figure 20 Solar simulator

The efficiency of a solar cell can be measured using a simple circuit comprising a solar cell, variable resistor, ammeter and voltmeter. Solar simulator is operated by projecting incident light with a constant light intensity on a solar cell. The resistor will be changed from zero to infinity to measure the voltage and current flowing through the resistor.

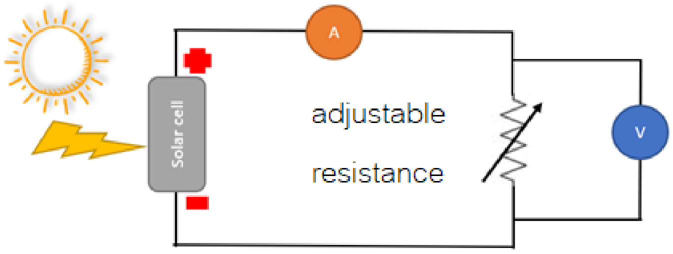

Figure 21 a simple circuit solar simulator

4. Literature review

4.1 Effect of $Pb(SCN)_2$ additive on perovskite solar cell performances

Tai et al. (2016) prepared perovskite film by two-step deposition method in a high humidity room. The $Pb(SCN)_2$ precursor was dissolved in DMSO at a concentration of 500 mg/ml, then spin-coating on a substrate with an m-TiO_2 layer was heated to 90 °C for 1 hour. Then, the MAI solution was span on the $Pb(SCN)_2$ film and the crystallize perovskite film was obtained. The structure of the assemble solar cell is FTO/c-TiO_2/m-TiO_2/perovskite/Spiro-MeOTAD/Au. The $MAPb(SCN)_xI_{3-x}$ perovskite solar cells, fabricated under humid air with 70% RH, represents a great average efficiency of 13.49% and optimum efficiency of 15%. In comparison with the pure $MAPbI_3$, the $MAPb(SCN)_xI_{3-x}$ perovskite solar cells shows better stability in humid condition. The solar cell efficiency maintained up to 86.7% of the initial value after 500 hours.

M. K. Kim et al. (2016) studied the addition of $Pb(SCN)_2$ precursor into $MAPbI_3$ solution with the concentration of 0, 0.1, 0.12, 0.15 and 0.18 mol. The result shows that, the addition of $Pb(SCN)_2$ to $MAPbI_3$ at a concentration of 0.15 mol yielded the best results and reached 90% more efficient than the pristine $MAPbI_3$ solar cell. The grain size of $MAPb(SCN)_xI_{3-x}$ perovskite were significantly larger than that of the pure $MAPbI_3$ from ~150 nm to ~5 μm as shown in Figure 3.

Ke et al. (2016) synthesized $MAPb(SCN)_xI_{3-x}$ perovskite films using one-step deposition method by adding $Pb(SCN)_2$ into $MAPbI_3$ solution with the concentration of 2.5, 5.0, 7.5 and 10%. The structure of the perovskite solar cell is FTO/SnO_2/perovskite/Spiro-OMeTAD/Au. The addition of Pb(SCN)2 increased the grain size of the perovskite film as seen in Figure 4. The addition of 5% of $Pb(SCN)_2$ in the $MAPbI_3$ solution can reduced the hysteresis and increased fill factor of the perovskite solar cells. This resulted in the higher power conversion efficiency (PCE) of the $MAPb(SCN)_xI_{3-x}$ perovskite solar cells (18.42%) than that of the $MAPbI_3$ solar cell (15.54%).

Yu et al. (2017) studied on the effect of $Pb(SCN)_2$ additive of 1 mol% into the $FA_{0.8}Cs_{0.2}Pb(I_{0.7}Br_{0.3})_3$ perovskite film. They reported that the crystal size of the perovskite film after the addition of 1 mol% of $Pb(SCN)_2$ increased larger from ~66 nm to ~1036 nm, as shown in Figure 22. The charge life was also three times longer than that of the reference one, from 330 nanoseconds to 1000 nanoseconds. The solar cell efficiency of the $Pb(SCN)_2$ additive perovskite film was increased from 13.44% to 17.68%.

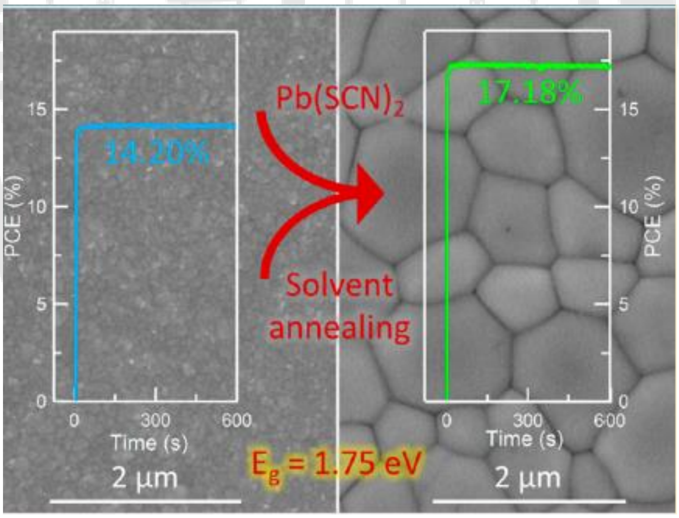

Figure 22 The SEM image the perovskite film after the addition of 1 mol% of $Pb(SCN)_2$ to the $FA_{0.8}Cs_{0.2}Pb(I_{0.7}Br_{0.3})_3$ perovskite film.

Source: Yu, Y., Wang, C., Grice, C. R., Shrestha, N., Zhao, D., Liao, W., . . . Yan, Y. (2017). Synergistic Effects of Lead Thiocyanate Additive and Solvent Annealing on the Performance of Wide-Bandgap Perovskite Solar Cells. *acs energy letters, 2*(5), 1177-1182. doi:10.1021/acsenergylett.7b00278

Cai, Wang, Sun, Li, and Xiao (2018) fabricated perovskite solar cells with the structure of FTO/c-TiO_2/m-TiO_2/perovskite/Spiro-OMeTAD/Au. The perovskite films used in the devices are prepared by doping $Pb(SCN)_2$ with the concentrations of 0, 1, 2, 3, 4 mol% into $FA_{0.8}Cs_{0.2}PbI_{2.68}Br_{0.32}$ perovskite films using one-step anti-solvent spin-coating method. The addition of $Pb(SCN)_2$ into the $FA_{0.8}Cs_{0.2}PbI_{2.68}Br_{0.32}$ perovskite films resulted in the larger grain-size perovskite films, less pinholes, continuous film surfaces and , long-life charge-transportation. Interestingly, the perovskite film with 2% of $Pb(SCN)_2$ additive reduced hysteresis effect and substantially improved the efficiency of the cells. The stability of solar cells was tested under ambient air with a humidity of 60 ± 5% for 45 days, the device retained 85.1% of its initial value with the maximum initial efficiency of 17.00%.

Kumlanwan et al. (2020) manipulated $MAPb(SCN)_xI_{3-x}$ perovskite films by doping $Pb(SCN)_2$ precursor into the MAI and PbI_2 solution with five various SCN^- levels (x = 0, 0.25, 0.5, 1 and 2) using a hot-casting method. They reported that the higher level of SCN^- substitution leads to the change of film's color from black to yellow including the increasing band gap from 1.59 eV ($CH_3NH_3PbI_3$ film) to 2.37 eV (CH_3NH_3 $Pb(SCN)_2I_1$ film). Consequently, the higher dopant of $Pb(SCN)_2$ successively decreased the solar cell efficiency. However, the $MAPb(SCN)_xI_{3-x}$ (x = 0.25, 0.5, 1 and 2) devices demonstrated the greater stability than that of the pure $CH_3NH_3PbI_3$ solar cell, and the best obtained cells efficiency is from $MAPb(SCN)_{0.5}I_{2.5}$ perovskite solar cell with the efficiency of 3.07%. They claimed that the presence of the hydrogen bonds between H and S and/or H and N in the $MAPb(SCN)_xI_{3-x}$ structures increases the perovskite film stability. Interestingly, the cell efficiency raised up to 11% of its initial value after 30 days storage.

4.2 The results of the one-step deposition method on the perovskite solar cells.

Zhao and Zhu (2014) reported the preparation of $MAPbCl_xI_{3-x}$ perovskite film from the mixed MACl with a MAI : PbI_2 : MACl ratio of 1 : 1 : x at x = 0 to 2 molar using one-step deposition method. The addition of MACl increased the crystal purity of $MAPbCl_xI_{3-x}$. As a result, the light absorption of the film is improved and the film coverage is more continuous and smoother than that of the pure $CH_3NH_3PbI_3$. This leads to the higher solar cell efficiency from 8% to 10%..

Chiang, Lin, and Wu (2016) prepared a mixed halide $CH_3NH_3PbI_{3-x-y}Br_xCl_y$ perovskite films using a one-step hot solution spin coating method. The inverted perovskite solar cell with structure: ITO/PEDOS:PSS/perovskite/PCBM/Al. The best solar cell efficiency is obtained from the ratio of PbI2, MABr, and MACl of 3 : 1 : 4. The multiple halogen elements resulted in a 16% improvement in solar cell efficiency.

Wang et al. (2016) synthesized perovskite films using the mixture of $PbCl_2$ and MAI with the concentration ratio of 3 : 1 molar in DMF solvent by one-step deposition. The solution was stirred over a night, then the films were deposited under ambient air with the humidity of 50±5 %. The films were annealed separately under ambient condition and under vacuum in order to analyze the different film properties between these two conditions. The inverted solar cells with the structure of ITO/PEDOS:PSS/perovskite/PCBM/C60/Al were assembled. The vacuum annealing was higher efficiency (12.98%) than that of the annealing at normal atmosphere (9.2%). This is because annealing sample in vacuum results in a continuous film covering the titanium surface.

4.3 The effects of carbon electrodes on the perovskite solar cells

Liu et al. (2020) assembled perovskite solar cells using carbon film (C) as a back electrode with the solar cell structure of FTO/c-TiO_2/m-TiO_2/perovskite/C. The carbon film was prepared with the mixture of carbon black, graphite, cellulose and medium, then it was coated onto FTO/c-TiO_2/m-TiO_2/perovskite layers by doctor blade method and annealed at the temperature of 100°C for 10 minutes. Carbon film layer was prepared by dissolved Ethyl acetate (CsAc) in IPA, then deposited the carbon film spin coating method and then heated to 60 °C for 5 min and at 100 °C for 10 min. They observed that the addition of Ethyl-acetate (CsAc) after cell assembly improved the fill factor (FF) and efficiency (15.6%) in comparing to the unfilled Ethyl Acetate (CsAc) (12.6%).

Bu et al. (2020) fabricated carbon-based perovskite solar cells. They had compared between the controlled carbon paste (C) and carbon paste with the addition of polyaniline and graphite (C-PANi/G). The PANi/G was prepared by adding graphite powder to 0.8 molar of aniline dissolved in hydrochloric acid (HCl) 1 molar, then the solution was mixed for 2 hours. After 2-hour mixing, the precursor will be added to the (0.8 M $NH_4)_2S_2O_8$ solution dissolved in hydrochloric acid (HCl) 1 molar. Then solution was stirred at the temperature of 0°C for 12 hours. The prepared PANi/G was washed by deionized water, ethanol and 2 molars of hydrochloric acid, respectively. Then, it was heated at the temperature of 60°C for 24 hours and grounded by Ball Mill machine for 12 hours. The PANi/G powder was obtained and it was added into carbon paste with the percentages of 1, 3, 5 and 7%wt, and was ball milling for 12 hours. The carbon paste with the addition of polyaniline and graphite (C-PANi/G) was obtained. The solar cells was constructed with the structures of FTO/c-TiO_2/m-TiO_2/ $CsPbBr_3$/C-PANi/G and FTO/c-TiO_2/m-TiO_2/ $CsPbBr_3$/C. The used of C-PANi/G significantly reduced charge recombination due to the lower CsPbBr3/C-PANi/G interlayer energy values. This induced the higher efficiency of the cells with the C-PANi/G back electrode (8.87%) than that of the cells with the conventional carbon electrode (6.17%). Moreover, the use of C-PANi/G electrode performed great stability with the efficiency retention of 93.5% of the initial value after stored under the humidity of 80% for 50 days.

Gong et al. (2020) studied the effect of adding carbon black between the perovskite layer and the carbon electrode. The adhesive carbon black (CB) was prepared by mixing carbon black, ethyl cellulose and terpinol. After that, the carbon black (CB) was screened on FTO/c-TiO_2/m-TiO_2/ $CsPbI_3Br$ layer, then the carbon electrode (CE) was deposited and was heated with the temperature of 100°C for 10 minutes. Accordingly, the solar cells with the structure of FTO/c-TiO_2/m-TiO_2/ $CsPbI_3Br$/CB/CE was achieved as seen in Figure 23, and the cell was sealed by polyolefin elastomer (POE). The carbon black (CB) nanoparticles was carried out into the perovskite film after leaving the cells for a while. The diffusion of these nanoparticles produces a large number of heterojunction structures, thereby improving the efficiency of the solar cell to 13.13%.

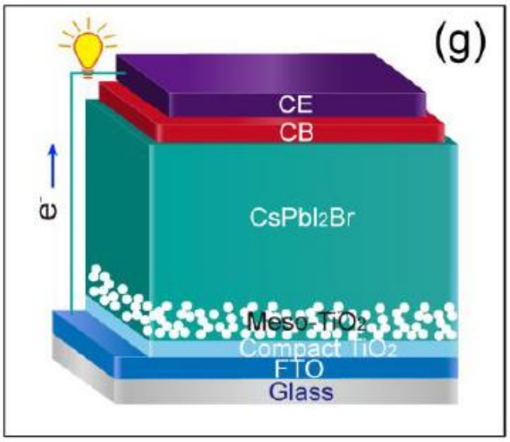

Figure 23 The structure of carbon-based perovskite solar cells with the addition of carbon black (CB) layer between perovskite layer and carbon electrode layer.

Source: Gong, S., Li, H., Chen, Z., Shou, C., Huang, M., & Yang, S. (2020). CsPbI2Br Perovskite Solar Cells Based on Carbon Black-Containing Counter Electrodes. *ACS Applied Materials & Interfaces, 12*(31), 34882-34889. doi:10.1021/acsami.0c0800

CHAPTER 3

RESEARCH METHODOLOGY

In this research, we prepared $CH_3NH_3Pb(SCN)_xI_{3-x}$ carbon-based hole-transport-layer-free perovskite solar cells according to the following steps.

1. Tools and chemicals.
2. Preparation of CH_3NH_3I, PbI_2 and $Pb(SCN)_2$ Precursors.
3. Preparation of working electrode.
4. Preparation of counter electrode.
5. Data Analyzation.

Tools and chemicals

1. The tools used in the experiment.

1.1 Solar simulator (model: XSS-5XD)

1.2 X-Ray diffraction (model: XRD, PANalytical, Empyrean, The Netherlands)

1.3 Scanning electron microscope (model: MiniSEM, SEC, SEN-4500M, Korea)

1.4 UV-VIS spectroscopy (model: UV-1800, Shimadzu, Japan)

1.5 Spin coating (model: Fly-dream, ST-V3)

1.6 Stirrer (model: IKA C-MAG HS 7)

1.7 Weighting machine (model: OHAUS, PA214)

1.8 Ultrasonic cleaner

1.9 Hot plate

1.10 micropipette

2. The chemicals used in the experiment.

Table 1 The chemicals used in the experiment.

No.	Chemicals	Company	Purity percentage
1	Lead (II) Thiocyanate, $Pb(SCN)_2$	Sigma-Aldrich	99.5%
2	Methylammonium iodide, CH_3NH_3I	Greatcell Solar	-
3	Lead (II) Iodide, PbI_2	Sigma-Aldrich	99%
4	TiO_2 paste 90T transparent	Greatcell Solar	
5	Titanium diisoproproxide bis(acetylacetonate), $C_{16}H_{26}O_6Ti$, 75 wt% in isopropanol	Sigma-Aldrich	-
6	2-propanol anhydrous, $(CH_3)_2CHOH$	Sigma-Aldrich	99.5%
7	Ethanol, C_2H_5OH	RCI Labscan	
8	N,N-Dimethylformamind anhydrous, C_3H_7NO		
9	Zinc dust < 10 µm, Zn	Sigma-Aldrich	$\geq$ 98%
10	Hydrochloric acid, HCl	RCI Labscan	37%
11	Poly(vinyl acetate)average Mw ~500,000 by GPC, $[(CH_2CH)O_2CCH_3]_n$	Sigma-Aldrich	-
12	Graphite flakes, C	Sigma-Aldrich	99%
13	Carbon Black	-	-
14	Ethyl acetate, $CH_3COOC_2H_5$	QRëC	99.5%
15	FTO (S-SnO_2 coated glass, sheet resistance of 15 ohm/sq)	Dyesol	
16	Dimethyl sulfoxide anhydrous	Sigma-Aldrich	$\geq$ 99.9%
17	Chlorobenzene anhydrous	Sigma-Aldrich	99.8%

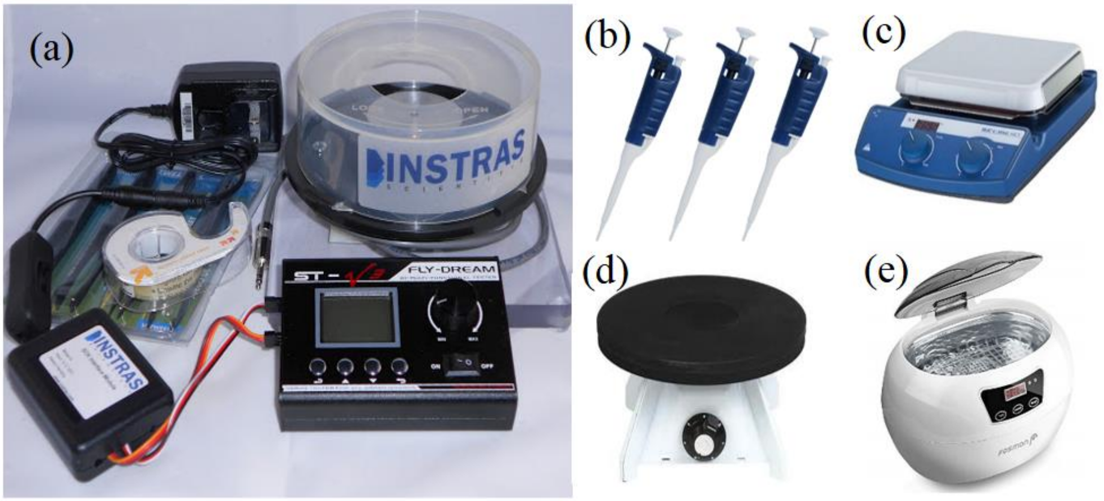

Figure 24 The examples of tools used in the experiment (a.) Spin coater (b.) Micropipettes (c.) Stirrer (d.) Hot plate and (e.) ultrasonic cleaner.

Figure 25 The chemicals used in the experiment (a.) MAI powder (b.) Pb(SCN)$_2$ powder (c.) PbI_2 powder (d.) Titanium diisoproproxide bis(acetylacetonate), 75 wt% in isopropanol (e.) Dimethyl sulfoxide anhydrous, DMSO (f.) N,N-Dimethylformamind anhydrous, DMF (g.) Ethanol and (h.) iO_2 paste 90T transparent.

Preparation of CH_3NH_3I, PbI_2 and $Pb(SCN)_2$ solutions

In this section, the CH_3NH_3I, PbI_2 and $Pb(SCN)_2$ solutions will be prepared for synthesizing $CH_3NH_3Pb(SCN)_xI_{3-x}$ films as light absorber on carbon-based hole-transport-layer-free perovskite solar cells. The $CH_3NH_3Pb(SCN)_xI_{3-x}$ films are performed in 6 different $Pb(SCN)_2$ concentrations, which are 0, 0.0375, 0.075, 0.1125, 0.15 and 0.3 molar. The preparation process of the CH_3NH_3I, PbI_2 and $Pb(SCN)_2$ solution as the bellowing steps.

1. Weight CH_3NH_3I powder (1.2 mol/mL) into 6 different bottles and assign as the number 1-6 on each bottle.

2. Weight PbI_2 powder with the 6 different molarities (1.2, 1.1625, 1.125, 1.0875, 1.05 and 0.9 molar), and add into the specified bottle from the bottle number 1-6 respectively.

3. Weight $Pb(SCN)_2$ powder with the 6 different molarities (0.0375, 0.075, 0.1125, 0.15 and 0.3 molar), and add into the specified bottle from the bottle number 2-6 respectively.

4. Add 1 mL of solvent, which is the admixture of N,N-Dimethylformamind anhydrous (DMF) and Dimethyl sulfoxide anhydrous (DMSO) of 9 : 1 into all the prepared bottles.

5. Stir these prepared solutions by magnetic stirrer at 60°C for 1 hour.

6. Filter CH_3NH_3I, PbI_2 and $Pb(SCN)_2$ solution by nylon syringe filter (0.22 micron).

The CH_3NH_3I, PbI_2 and $Pb(SCN)_2$ solutions with 6 different concentrations of $Pb(SCN)_2$ additive (0.0375, 0.075, 0.1125, 0.15 and 0.3 molar) are completed as illustrated in Figure 26

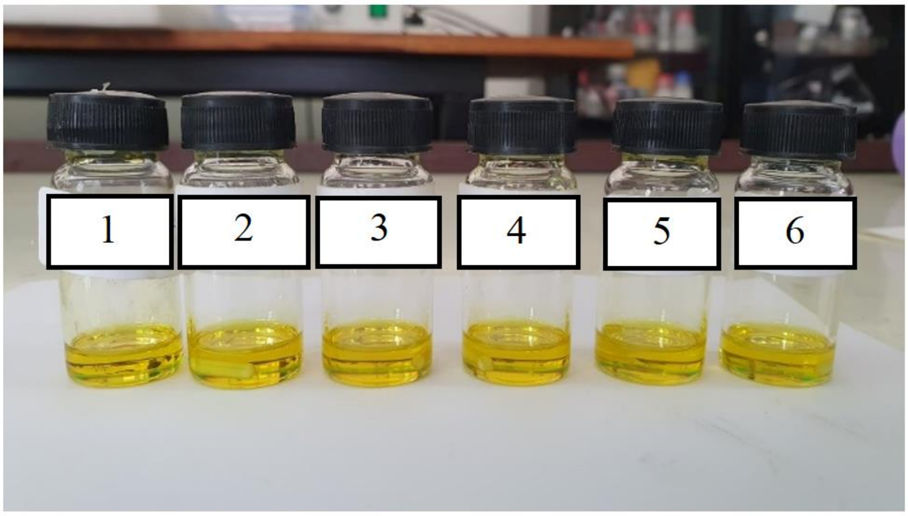

Figure 26 The CH_3NH_3I, PbI_2 and $Pb(SCN)_2$ solutions with 6 different $Pb(SCN)_2$ additions of (1) 0, (2) 0.0375, (3) 0.075, (4) 0.1125, (5) 0.15 and (6) 0.3 molar.

Preparation of working electrode

In this topic, the preparation of working electrode is separated into 2 sections, which are the FTO glass preparation and the TiO_2 film preparation.

1. FTO glass preparation

The FTO glass (Fluorine dopped tin oxide glass) is one of the most essential part of the perovskite solar cells' fabrication because FTO glass is used as the transparent substrate. The FTO glass must be cleaned before the film deposition. The process of preparing conductive glass is listed as follows.

1) Cut the conductive glass to a size of 2 x 2 square centimeters, then attach the capton tape onto the surface of the conductive glass as shown in Figure 27.

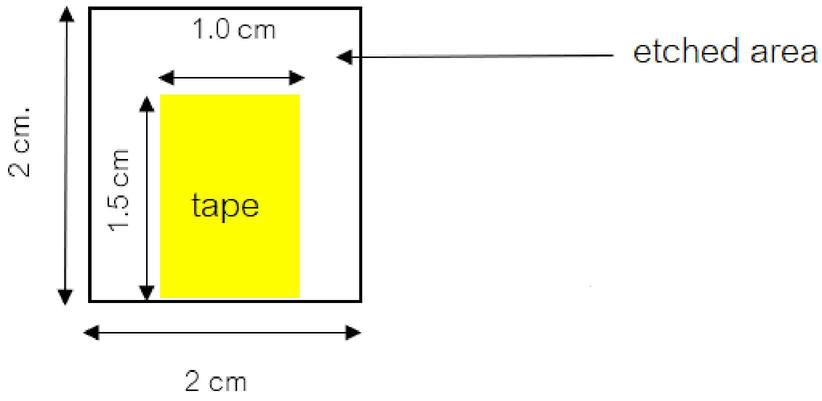

Figure 27 the schematic of FTO glass

2) Mix the zinc powder (Zn) with deionized water, stir until it forms a paste, then apply it to the etched area on the FTO conductive glass surface (the area where the capton tape is not attached, as seen in figure 27). Next, 3.0 molar hydrochloric acid (HCl) was applied onto the Zn-applied area, waiting for the HCl to complete the chemical reaction with Zn, then wiped the surface with a cotton.

3) Clean the processed FTO glass using dishwashing liquid, water, deionized water and ethanol, by vibrating in the ultrasonic in each step for 15 minutes, respectively. After that, the FTO was dried using hair dryer.

After these processes, the cleaned and patterned FTO glass is obtained as showed in Figure 28, and it is ready for the film deposition in the next step.

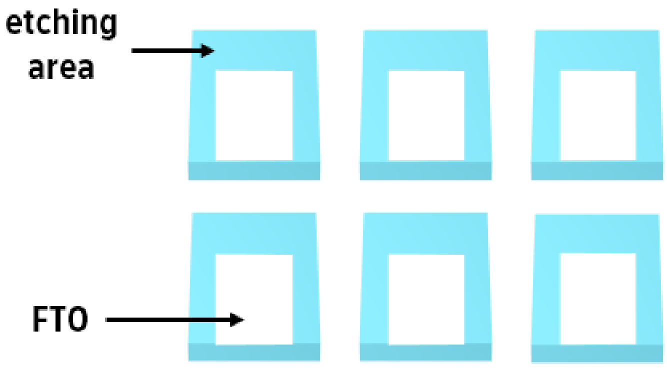

Figure 28 cleaned and patterned FTO glass

2. Procedure for preparing the working electrode

The working electrode in our work consists of 3 essential layers, which are 1) Blocking layer (Bl-TiO_2) is the first layer that is coated on the conductive glass 2) Mesoporous-Titanium Dioxide layer (mp-TiO_2) is an electron transport layer, which helps to disperse electrons from perovskite layer and transfer the electrons' collector and 3) Perovskite layer or light absorption layer is the layer that harvests sunlight in the perovskite solar cell device. The processes of deposition each layer are described as follows.

2.1 The blocking layer (Bl-TiO_2) preparation

1) Filtered Titanium diisoproproxide bis(acetylacetonate) solution with a 0.22-micron nylon syringe filter and stirred by magnetic stirrer for 1 hour.

2) Attach the capton tape (4 mm) to the surface of the prepared FTO glass to limit the active area of the solar cell as seen in Figure 29.

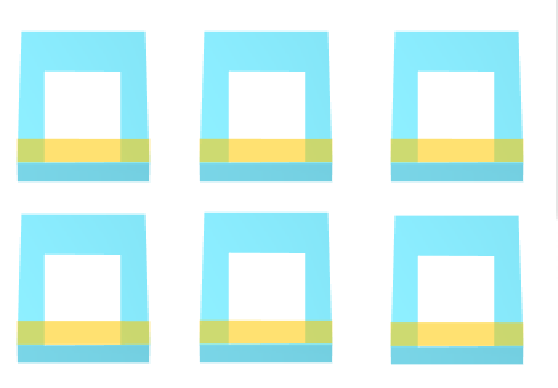

Figure 29 the FTO glass attached by capton tape.

3) Coated the Titanium diisoproproxide bis(acetylacetonate) solution onto the prepared FTO glass by spin coater at 3000 rpm for 45 seconds and heated to 120 °C for 10 min. After cooling down the film to room temperature, Titanium diisoproproxide bis(acetylacetonate) solution was repeatedly deposited on the first layer one more time.

4) The FTO glass with titanium layer was dried at 125°C for 10 minutes. After that, the capton tape was removed from the FTO glass, and then the film was sintered at 500°C for 1 hour to obtain a blocking TiO_2 layer on the conductive glass.

Consequently, the blocking layer (Bl-TiO_2) is accomplished after this process, and the blocking layer preparation process is summarized in Figure 30.

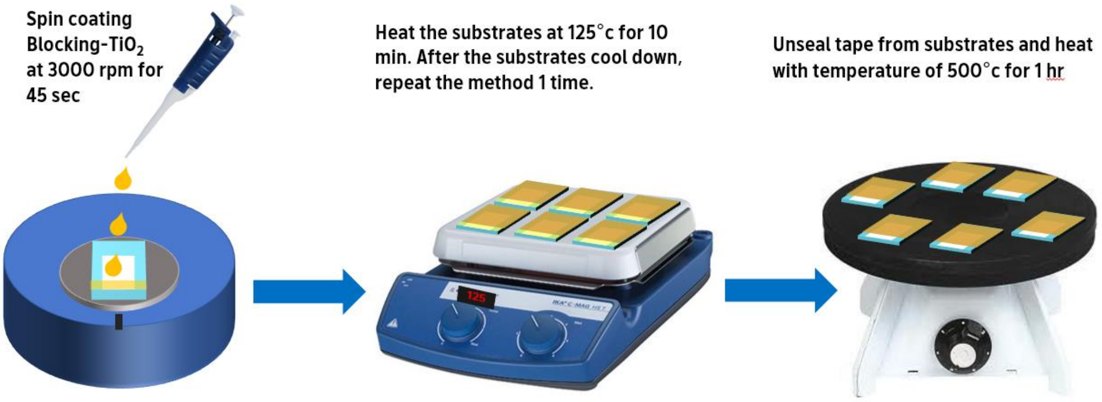

Figure 30 The summary of blocking layer preparation process.

2.2 The mesoporous TiO_2 layer preparation process

1) Dissolve 1.65 g of TiO_2 paste 90T transparent (particle size 20 nm) in 5 ml of ethanol, and shake until the solution become homogeneous.

2) Apply capton tape (4 mm) at the same position as seen in figure 29 on the surface of the prepared FTO/Bl- TiO_2 layer to limit the working electrode area.

3) Deposit the mesoporous-TiO_2 solution on the prepared FTO/Bl- TiO_2 by spin coating deposition at 4000 rpm for 45 seconds and heated to 80 °C for 10 minutes.

4) Remove the capton tape from FTO glass from step 3) and sinter samples at the temperature of 500°C for 1 hour.

As a result, the FTO/Bl- TiO_2/mp-TiO_2 was obtained, and the process of the mesoporous-TiO_2 deposition method is represented in Figure 31.

Figure 31 The summary of mesoporous-TiO_2 deposition method

2.3) The preparation process of perovskite layer

1) Attach capton tape (5 mm) at the same position as seen in Figure 29 to limit the working electrode area on the prepared FTO/Bl- TiO_2/mp-TiO_2 substrate.

2) Deposit the 6 different CH_3NH_3I, PbI_2 and $Pb(SCN)_2$ solutions on the prepared FTO/Bl- TiO_2/mp-TiO_2 substrates using a hot-casting method by heating the substrates at 145°C for 2 minutes prior to film coating, then spin coating the solutions onto the substrates at 3000 rpm for 30 seconds. Films were heated to 120 °C for 10 minutes, as a consequence the $CH_3NH_3Pb(SCN)_xI_{3-x}$ films at x = 0, 0.0625, 0.125, 0.1875, 0.25 and 0.5 are obtained with the grey-black film's color as shown in Figure 32.

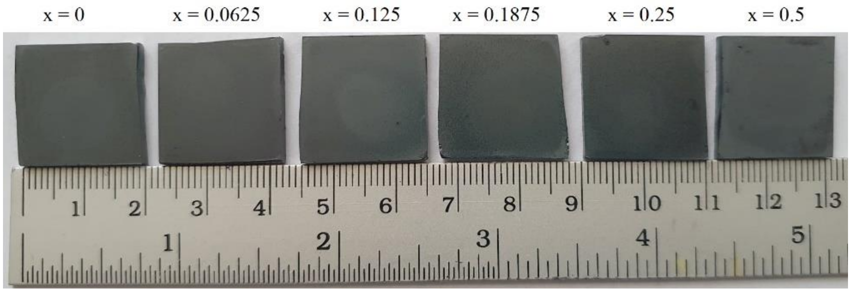

Figure 32 Optical images of $CH_3NH_3Pb(SCN)_xI_{3-x}$ Films (x = 0, 0.0625, 0.125, 0.1875, 0.25 and 0.5).

The process of preparing perovskite layer is shown in Figure 33.

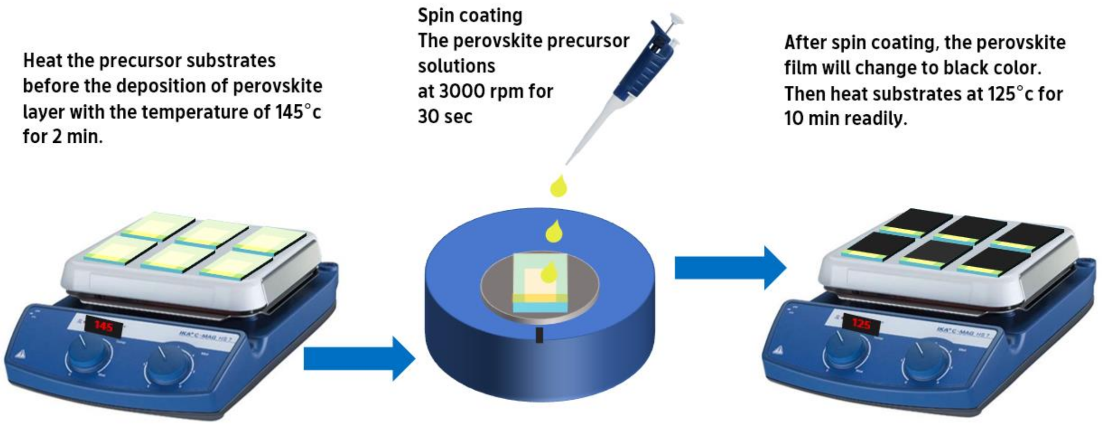

Figure 33 The conclusion of preparation process of perovskite layer

Procedure of preparing the counter electrode

In this work, the perovskite solar cells will be assembled using carbon film as the counter electrode. The preparation of counter electrode will be discussed in this topic as the following steps.

1. Preparation of carbon paste

1.1 Dissolve 2.5 g of polyvinyl acetate (PVAc) in Ethyl acetate (EA) 30 ml, and stir the solution at the temperature of 50°C using magnetic stirrer until the solution become homogenous.

1.2 Mix 2 g of carbon black and 6 g of graphite into the PVAc solution, and stir the mixture at 80°C until it becomes homogenous solution. Afterwards, the solution was dried at the 80°C until the solution becomes powder.

1.3 Add Chlorobenzene 30 ml to the mixture in number (1.2), and stir the solution at 80°C for 1 h. Then, the solution is evaporated for 7 days.

2. Preparation of counter electrode

2.1 Cutting FTO into the size of 2x2 square-centimeter and cleaning the FTO in detergent water, water, deionized water and ethanol by ultrasonic cleaner for 15 minutes per each step, respectively.

2.2 Tape the FTO substrates with 0.5 centimeters from the edges as shown in figure 34. Then, screen carbon paste, which is prepared in step 1, onto the FTO surface.

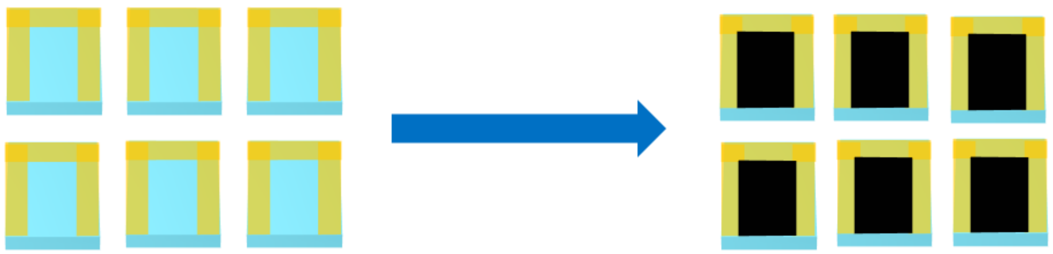

Figure 34 the preparation of counter electrode

2.3 Remove the tape from substrates after painted carbon paste and articulate them to the working electrode substrates. After that, clip these 2 glasses (working electrode and counter electrode) together as seen in figure 35. Finally, the carbon-based hole-transport-layer-free perovskite solar cells are completed.

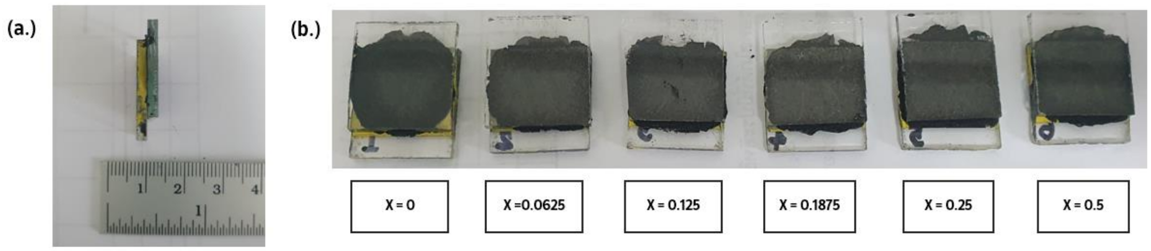

Figure 35 (a) Side-view and (b) top view of carbon-based hole-transport-layer-free perovskite solar cells.

The carbon-based hole-transport-layer-free $CH_3NH_3Pb(SCN)_xI_{3-x}$ perovskite solar cells will be dried under room temperature for 3 days. The performance of the perovskite solar cells will be characterized by solar simulator for 30 days. The schematic of the carbon-based hole-transport-layer-free $CH_3NH_3Pb(SCN)_xI_{3-x}$ perovskite solar cell is shown in figure 36.

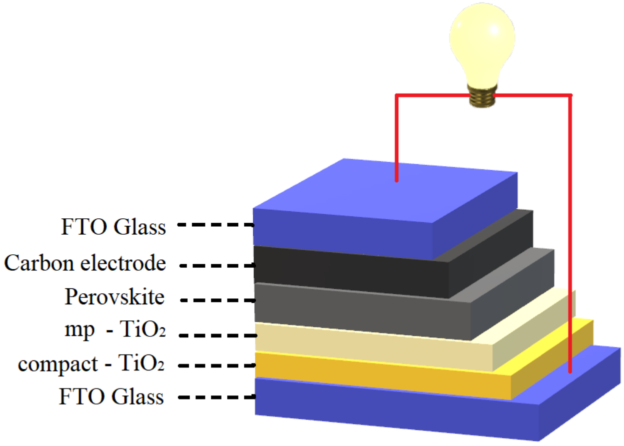

Figure 36 The schematic structure of carbon-based hole-transport-layer-free $CH_3NH_3Pb(SCN)_xI_{3-x}$ perovskite solar cell.

CHAPTER 4

RESULT

In this research, we studied the effects of doping SCN^- moiety into $CH_3NH_3Pb(SCN)_xI_{3-x}$ perovskite films at x = 0, 0.0625, 0.125, 0.1875, 0.25 and 0.5 on the morphology, crystallinity and absorption of $CH_3NH_3Pb(SCN)_xI_{3-x}$ films. The $CH_3NH_3Pb(SCN)_xI_{3-x}$ perovskite films are analyzed by scanning electron microscope (SEM), X-Ray diffraction technique (XRD) and UV-Vis spectroscopy, respectively. The efficiency and stability of the carbon-based hole-transport-layer-free $CH_3NH_3Pb(SCN)_xI_{3-x}$ perovskite solar cells were characterized using solar simulator. The results are analyzed as follows.

4.1 Analyzation of $CH_3NH_3Pb(SCN)_xI_{3-x}$ perovskite films.

4.1.1 Optical images of $CH_3NH_3Pb(SCN)_xI_{3-x}$ perovskite films.

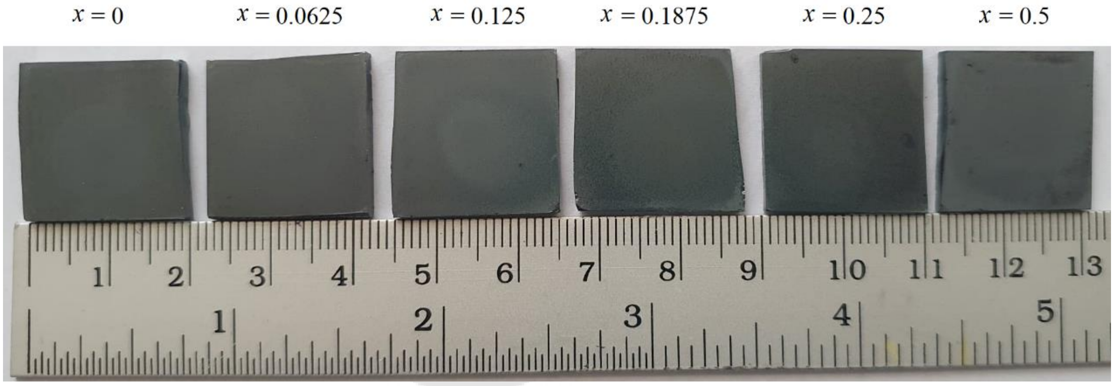

Figure 37 Optical images of $CH_3NH_3Pb(SCN)_xI_{3-x}$ perovskite films.

$CH_3NH_3Pb(SCN)_xI_{3-x}$ perovskite films (x = 0, 0.0625, 0.125, 0.1875, 0.25 and 0.5) are deposited on the TiO_2 layer by the hot-casting method. The optical images were taken immediately after preparation, and the $CH_3NH_3Pb(SCN)_xI_{3-x}$ films showed a black-dark grey color as seen in figure 37.

4.1.2 Surface morphology of $CH_3NH_3Pb(SCN)_xI_{3-x}$ perovskite films.

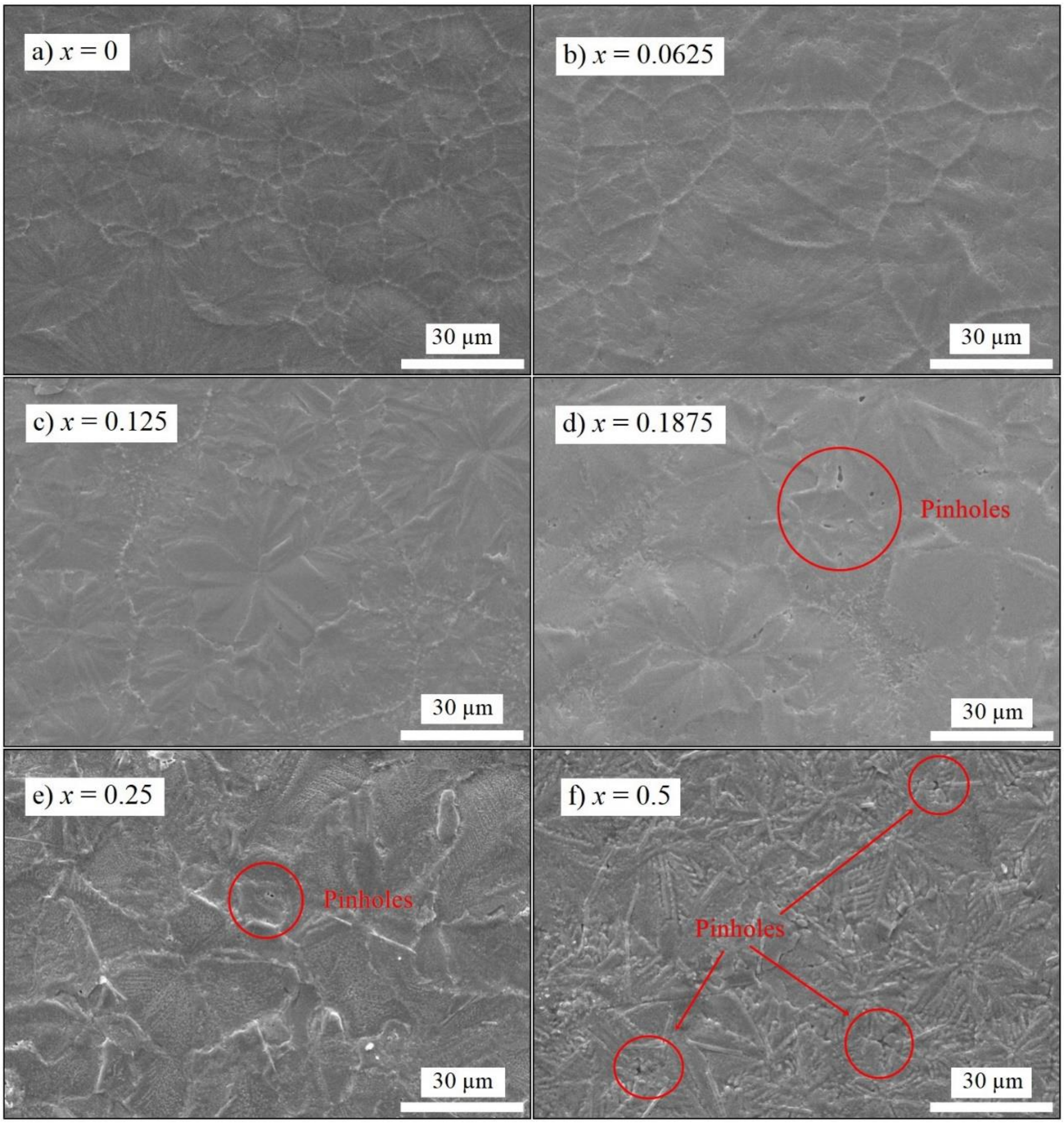

Figure 38 Top-view of SEM images of $CH_3NH_3Pb(SCN)_xI_{3-x}$ perovskite films at x = (a) 0, (b) 0.0625, (c) 0.125, (d) 0.1875, (e) 0.25 and (d) 0.5.

The surface morphology of $CH_3NH_3Pb(SCN)_xI_{3-x}$ perovskite films (x = 0, 0.0625, 0.125, 0.1875, 0.25 and 0.5) was obtained using Mini Scanning Electron Microscopy (Mini-SEM, SEC, SEN-4500M, Korea) at department of science, Khon Kaen university. The results show that the surface morphology of the pure $CH_3NH_3PbI_3$ (x = 0) film in figure 38 (a) is smooth, continuous and pinhole-free with average grain size of 12.83 ± 6.66 μm. Interestingly, the small addition of $Pb(SCN)_2$ in CH_3NH_3I/PbI_2 solution enlarged $CH_3NH_3Pb(SCN)_xI_{3-x}$ grain sizes as seen in figure 38(b-f). The surfaces morphology of $CH_3NH_3Pb(SCN)_xI_{3-x}$ films at x = 0.0625 and x = 0.125, figure 38(b-c), are continuous, smooth and pinhole-free as same as the pure $CH_3NH_3PbI_3$ (x = 0) film. However, the $CH_3NH_3Pb(SCN)_xI_{3-x}$ films at x = 0.1875 and x = 0.25, figure 38(d-e), showed many pinholes on their surfaces, also represented the change on the grain structures. Lastly, the high dopant of SCN^- at x = 0.5 induced surface roughness and formation of rod-like structures on the film as seen in figure 38(f). Kumlangwan et al. (2020) studied the high SCN^- dopant ratio on $CH_3NH_3Pb(SCN)_xI_{3-x}$ films above x = 0.25, and they observed the high SCN- dopant levels above x = 0.25 causes the rod-like structures formation on the $CH_3NH_3Pb(SCN)_xI_{3-x}$ film surfaces.

4.1.3 Thickness of $CH_3NH_3Pb(SCN)_xI_{3-x}$ perovskite films.

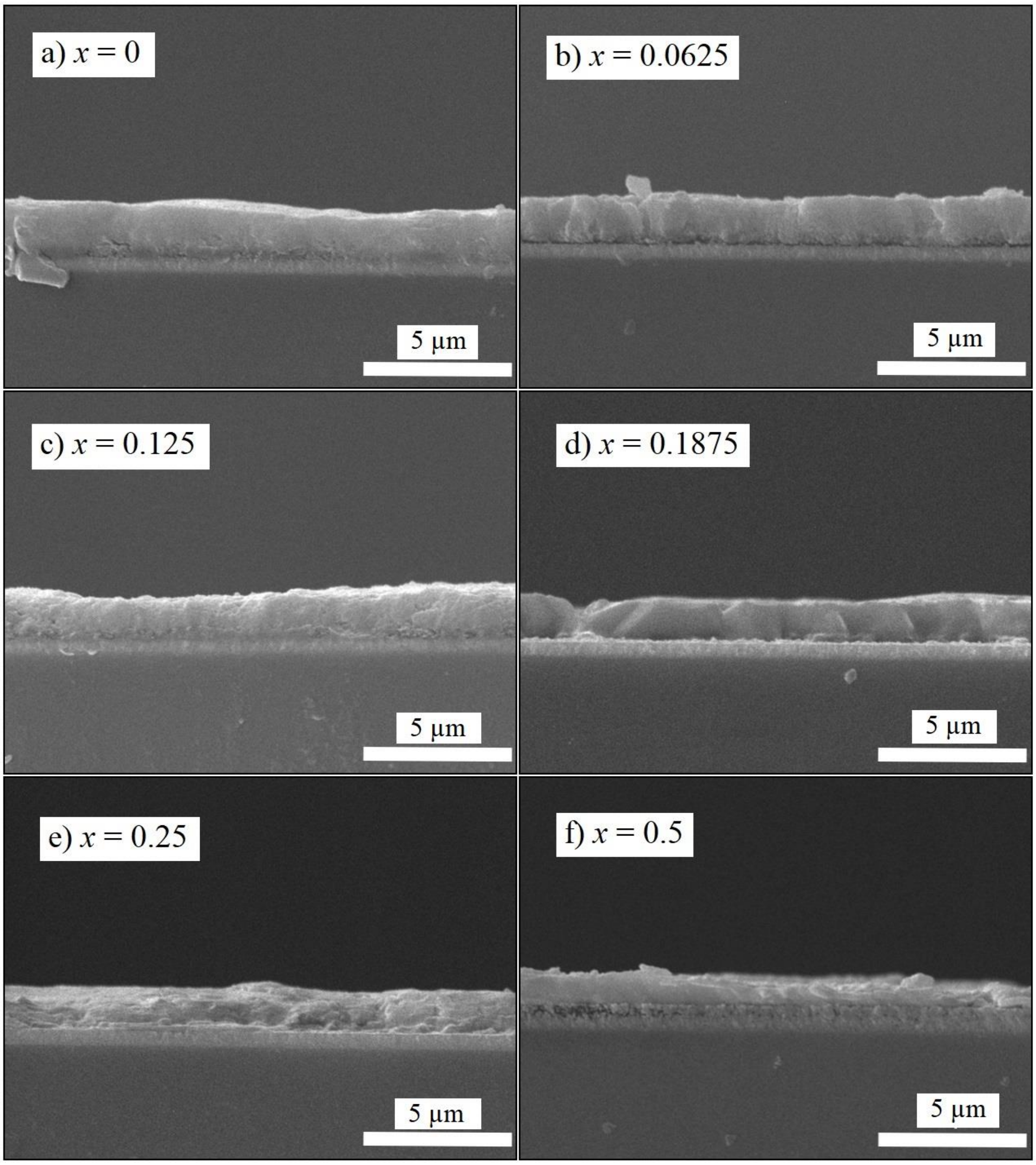

Figure 39 Cross-sectional view of SEM images of $CH_3NH_3Pb(SCN)_xI_{3-x}$ perovskite films at x = (a) 0, (b) 0.0625, (c) 0.125, (d) 0.1875, (e) 0.25 and (d) 0.5.

The cross-sectional view of SEM images of $CH_3NH_3Pb(SCN)_xI_{3-x}$ perovskite films (x = 0, 0.0625, 0.125, 0.1875, 0.25 and 0.5) were also measured by Mini Scanning Electron Microscopy (Mini-SEM, SEC, SEN-4500M, Korea) as same as the surface images. The cross-sectional view of SEM images in figure 39(a-f) represented the thickness of $CH_3NH_3Pb(SCN)_xI_{3-x}$ perovskite films about 1.81 ± 0.14 μm, 1.63 ± 0.09 μm, 1.64 ± 0.18 μm, 1.46 ± 0.09 μm, 1.45 ± 0.11 μm and 1.06 ± 0.12 μm for x = 0, 0.0625, 0.125, 0.1875, 0.25 and 0.5, respectively. This information indicates that the thickness of $CH_3NH_3Pb(SCN)_xI_{3-x}$ perovskite films tend to decrease with the increasing of SCN^- dopant matter. It is possibly due to a lower viscosity of the solution with higher $Pb(SCN)_2$ concentration causing more spin-out of the solution. During the solution process, we found that the addition of $Pb(SCN)_2$ into CH_3NH_3I/PbI_2 solutions urged CH_3NH_3I and PbI_2 dissolution.

4.1.4 Crystal structure of $CH_3NH_3Pb(SCN)_xI_{3-x}$ perovskite films.

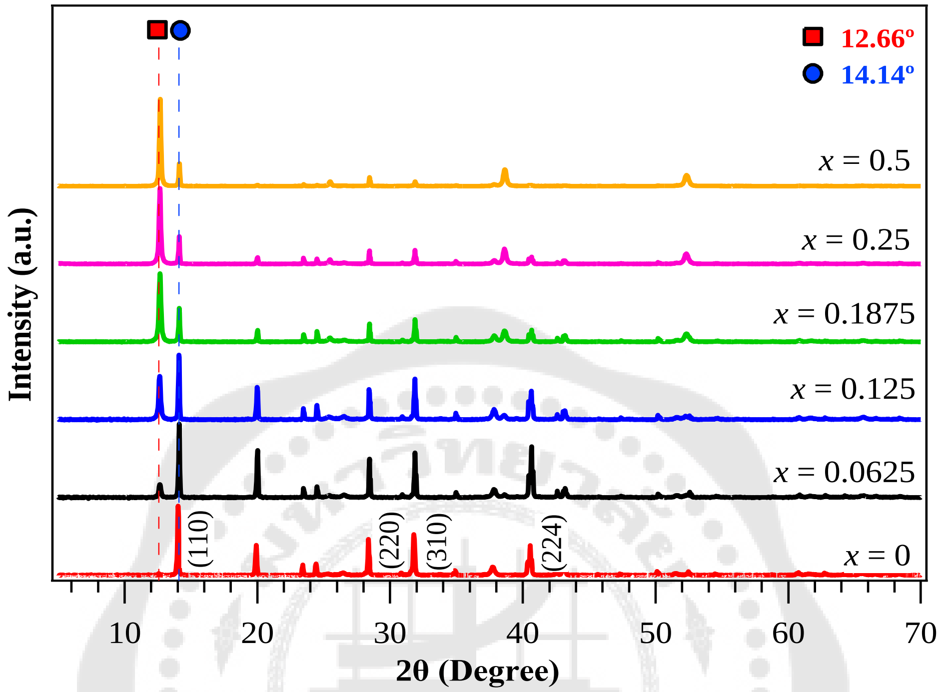

Figure 40 XRD pattern of $CH_3NH_3Pb(SCN)_xI_{3-x}$ perovskite films (x = 0, 0.0625, 0.125, 0.1875, 0.25 and 0.5)

The crystal structures of the prepared $CH_3NH_3Pb(SCN)_xI_{3-x}$ films at x = 0, 0.0625, 0.125, 0.1875, 0.25 and 0.5 were studied from XRD measurements, as indicated in figure 40. The XRD measuring was performed at department of science, Khon Kean university using X-Ray diffraction model PANalytical, EMPYREAN made in the Netherlands. The $CH_3NH_3Pb(SCN)_xI_{3-x}$ films were measured one day after the deposition. The $CH_3NH_3Pb(SCN)_xI_{3-x}$ films were coated on the TiO_2 film, and the with the structure of FTO/compact-TiO_2/mp-TiO_2/$CH_3NH_3Pb(SCN)_xI_{3-x}$, respectively. The results show that, the diffraction peaks of the pure $CH_3NH_3PbI_3$ ($x = 0$) film appear at 14.14°, 28.47° and 31.90° corresponded to the (110), (220) and (310) planes of the tetragonal $CH_3NH_3PbI_3$ perovskite structure, respectively. Likewise, Kumlangwan et al. (2020) studied the high dopant of $Pb(SCN)_2$ into CH_3NH_3I/PbI_2 precursors, the diffraction peaks of the $CH_3NH_3PbI_3$ films also appear at 14.09°, 28.39° and 31.82° and indexed to the (110), (220) and (310) planes of the tetragonal $CH_3NH_3PbI_3$ perovskite structure. XRD spectra of $CH_3NH_3Pb(SCN)_xI_{3-x}$ films at $x = 0.0625$, 0.125, 0.1875, 0.25 and 0.5 present diffraction angles at 14.11°, 28.44° and 31.88° are assigned as (110), (220) and (310) planes, which is slightly different from a pure $CH_3NH_3PbI_3$ film. However, a new peak at 12.66° was also detected from $CH_3NH_3Pb(SCN)_xI_{3-x}$ films for all SCN^- doped films. The 12.66° peak intensity is splendidly increased with SCN^- dopant level, as seen in Figure 40. To further understanding, the $CH_3NH_3Pb(SCN)_xI_{3-x}$ peaks were compared with the precursors data base as represented in Figure 41. It is clear seen that the 12.66° peak could possibly be influenced by the remaining PbI_2 because the main XRD peak of PbI_2 presents at 12.66°. Correspondingly, Chen et al. (2015) studied the addition of small amount of $Pb(SCN)_2$ into PbI_2 using two-step deposition. They detected the diffraction peaks of $CH_3NH_3Pb(SCN)_xI_{3-x}$ films at 14.10°, 28.47° and 31.93° and the residue PbI_2 at 12.58°.

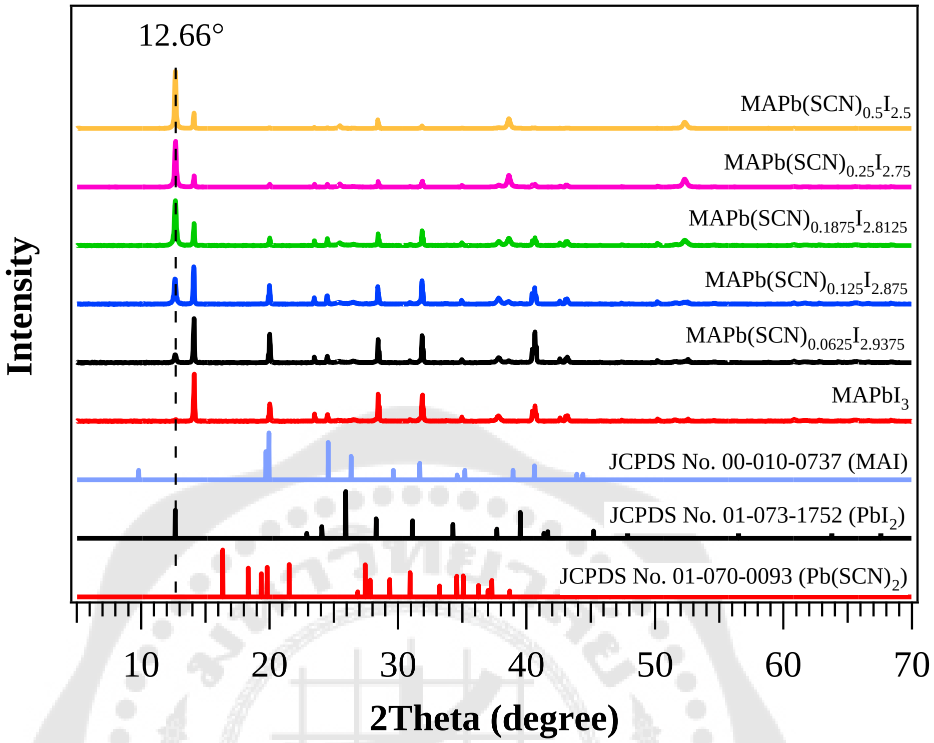

Figure 41 XRD pattern of $CH_3NH_3Pb(SCN)_xI_{3-x}$ perovskite films (x = 0, 0.0625, 0.125, 0.1875, 0.25 and 0.5) and the JCPDS of CH_3NH_3I (MAI), PbI_2 and $Pb(SCN)_2$ precursors

4.1.5 The optical properties of $CH_3NH_3Pb(SCN)_xI_{3-x}$ films

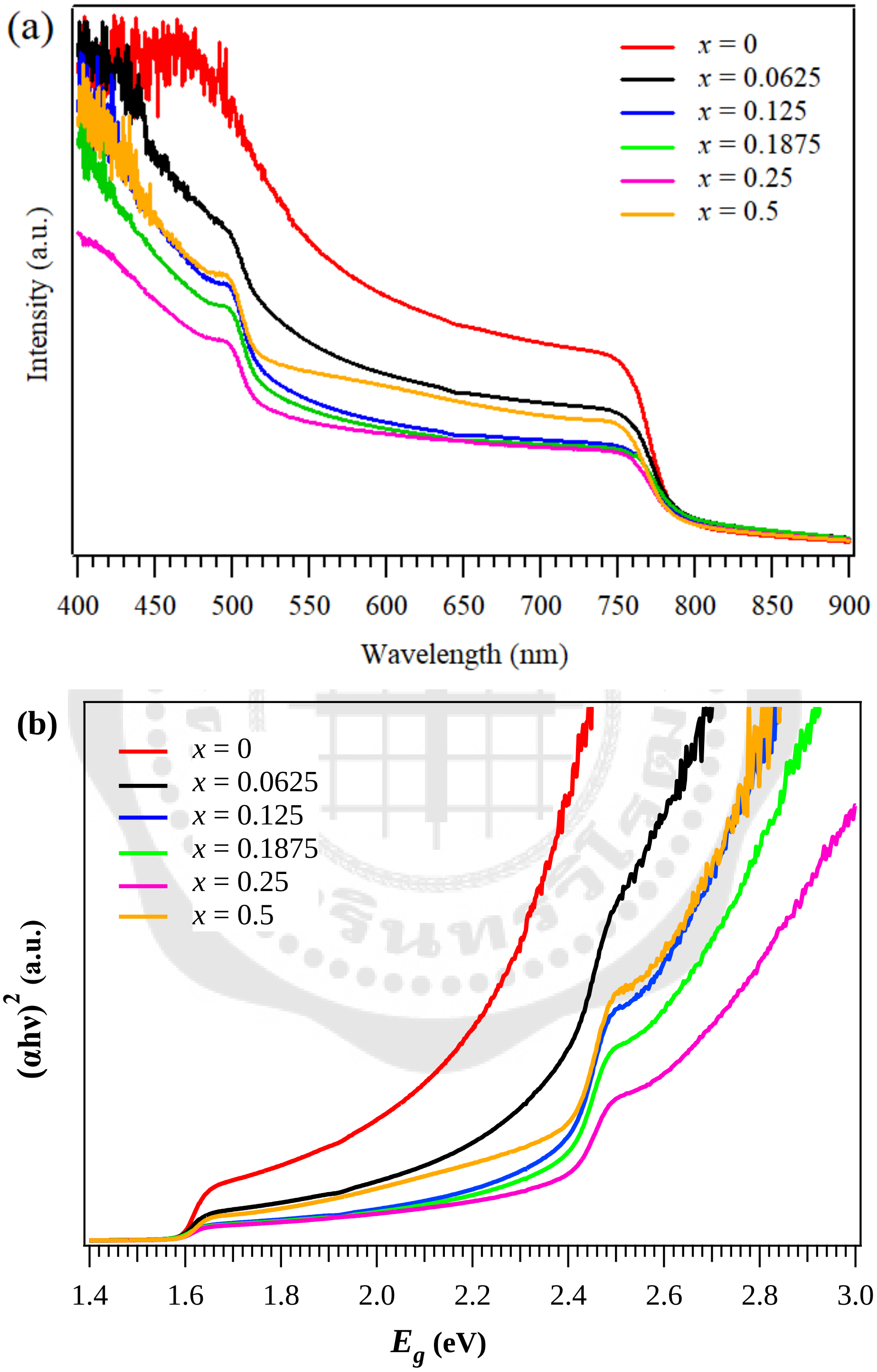

Figure 42 (a) UV-Vis absorbance spectra and (b) Tauc plots of the prepared $CH_3NH_3Pb(SCN)_xI_{3-x}$ films at x = 0, 0.0625, 0.125, 0.1875, 0.25 and 0.5.

The optical properties of $CH_3NH_3Pb(SCN)_xI_{3-x}$ films were analyzed using UV-Vis spectroscopy. The absorbance spectra in Figure 42(a) show similar optical absorbance edges around 780-790 nm for all six $CH_3NH_3Pb(SCN)_xI_{3-x}$ films. Nevertheless, the absorbance intensity of $CH_3NH_3Pb(SCN)_xI_{3-x}$ films decreases with an increasing SCN^- dopant level. The optical bandgaps (E_g) were anticipated from the Tuac plots in Figure 42(b). Straight-lines were drawn on enlarged Tuac plots in Figure 43(a-f) to estimate the bandgap values. These values are listed in Table 2. The bandgap of the $CH_3NH_3PbI_3$ (x = 0) film in this work is approximately 1.59 eV, which is closed to the reported values of 1.50 - 1.59 eV (Halder et al., 2015; Q. Jiang et al., 2015; Kumlangwan et al., 2020). Likewise, the values of the energy bandgap of five $CH_3NH_3Pb(SCN)_xI_{3-x}$ films are similar to that of the pure MAPbI3 (x = 0) film. Halder et al. (2015) studied the comparison between the $CH_3NH_3Pb(SCN)_xI_{3-x}$ perovskite solar cell and the pure $CH_3NH_3PbI_3$ perovskite solar cell. The optical absorption of the $CH_3NH_3Pb(SCN)_xI_{3-x}$ and $CH_3NH_3PbI_3$ films were analyzed using photoluminescence emission spectroscopy (PL spectroscopy), the result showed that the absorption band edge onset of the pristine $CH_3NH_3PbI_3$ film is located at ~790 nm, which is corresponded to bandgap of 1.57 eV. However, the absorption band edge of the doping $CH_3NH_3PbI_3$ with SCN^- has a blue shift of ~40 nm, which is corresponded to 1.65 eV. Qinglong Jiang et al. (2015) determined the optical bandgap of that $CH_3NH_3PbI_3$ and $CH_3NH_3Pb(SCN)_2I_1$ thin films by plotting the square of the Kubelka-Munk function $\left[F\left(R_\infty\right)\times\left(h\nu\right)\right]$ versus $h\nu$. The bandgap of $CH_3NH_3PbI_3$ film was determined to be 1.504 eV. In contrast, $CH_3NH_3Pb(SCN)_2I_1$ thin films exhibited a gradually wider bandgap of 1.532 eV. The absorbance intensity (Figure 42(b)) decreases with the increasing SCN^- level. This should be due to decreasing film thickness (observed in the cross-sectional SEM of Figure. 39).

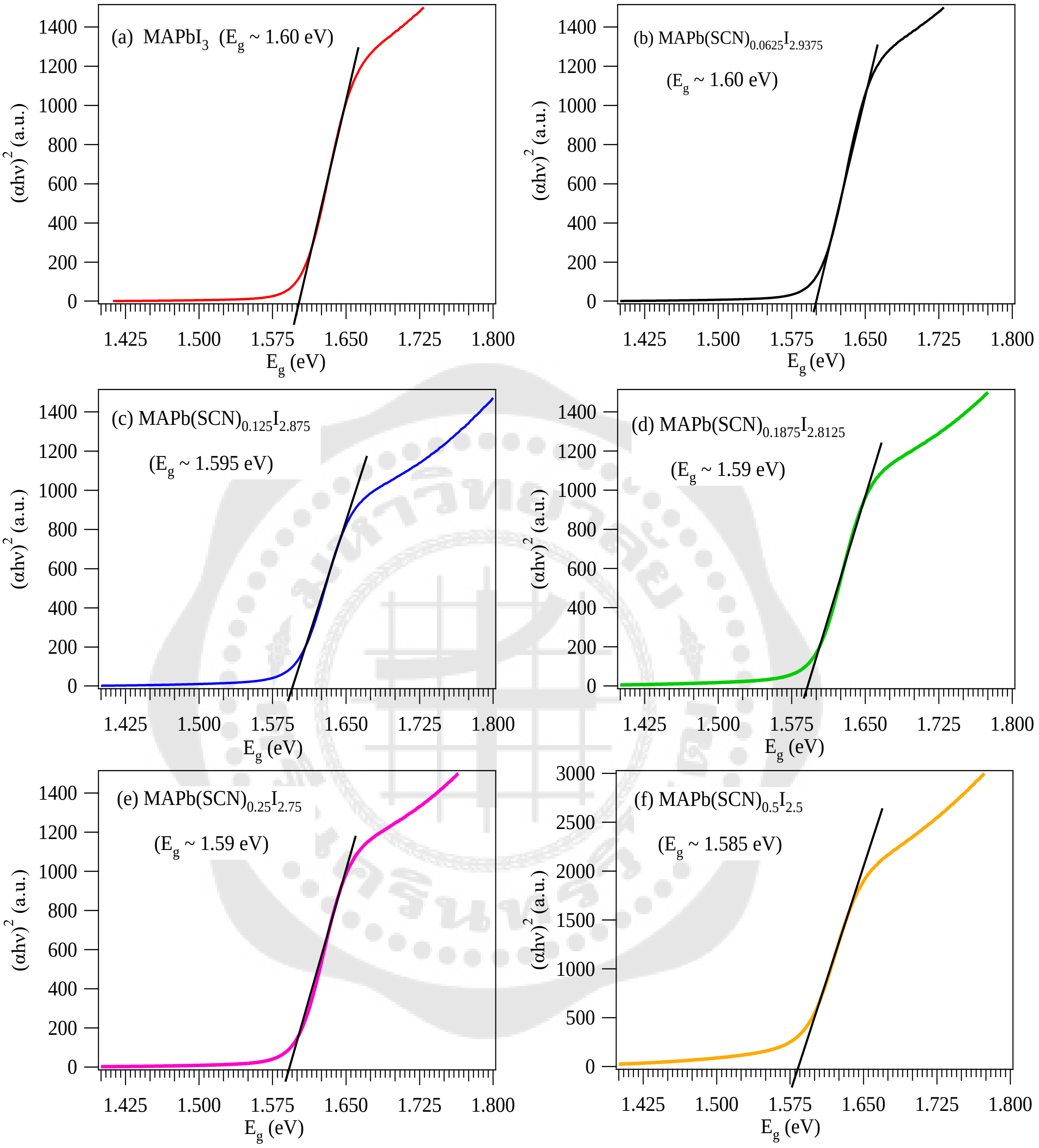

Figure 43 The enlarged Tauc plot from Figure 42(b) for estimating the energy bandgap (E_g) of the prepared $CH_3NH_3Pb(SCN)_xI_{3-x}$ films.

Table 2 The calculated and experimental bandgaps (E_g) of $MAPb(SCN)_xI_{3-x}$ films.

Samples	Energy gap (eV)
$MAPbI_3$	1.600
$MAPb(SCN)_{0.0625}I_{2.9375}$	1.600
$MAPb(SCN)_{0.125}I_{2.875}$	1.595
$MAPb(SCN)_{0.1875}I_{2.8125}$	1.590
$MAPb(SCN)_{0.25}I_{2.75}$	1.590
$MAPb(SCN)_{0.5}I_{2.5}$	1.585

4.2 Characterization of $CH_3NH_3Pb(SCN)_xI_{3-x}$ perovskite solar cells.

4.2.1 Performances of $CH_3NH_3Pb(SCN)_xI_{3-x}$ perovskite solar cells

$CH_3NH_3Pb(SCN)_xI_{3-x}$ perovskite films were used as a light absorption layer in carbon-based HTL-free perovskite solar cells. The architecture of these carbon-based HTL-free solar cells consists of FTO/bl-TiO_2/mp-TiO_2/$CH_3NH_3Pb(SCN)_xI_{3-x}$/carbon/FTO, as illustrated in Figure 44(a). Prior to the efficiency measurements, the carbon-based HTL-free solar cells were left for 3 days to completely dry the carbon pastes. The performance of these carbon-based HTL-free $CH_3NH_3Pb(SCN)_xI_{3-x}$ devices was measured under a simulated sunlight intensity of 100 mWcm^{-2} at 1.5 AM. Photocurrent (J) versus photovoltage (V) curves of the carbon-based HTL-free $CH_3NH_3Pb(SCN)_xI_{3-x}$ solar cells are shown in Figure 44(b). The open-circuit voltage (V_{oc}), short-circuit current density (J_{sc}), fill-factor (FF) and efficiency (η) of these devices were extracted from the J-V curves and listed in Table 3. As a result from J-V curve, the value of short-circuit current density (J_{sc}) of the carbon-based HTL-free $CH_3NH_3Pb(SCN)_xI_{3-x}$ solar cells are 21.59 mA/cm^2, 16.52 mA/cm^2, 12.64 mA/cm^2, 10.15 mA/cm^2, 10.60 mA/cm^2 and 7.84 mA/cm^2 for the carbon-based HTL-free $CH_3NH_3Pb(SCN)_xI_{3-x}$ devices at = 0, 0.0625, 0.125, 0.1875, 0.25 and 0.5, respectively. The open-circuit voltage (V_{oc}) retrieved from J-V curve are 0.95 V, 0.79 V, 0.78 V, 0.82 V, 0.59 V and 0.60 V for the carbon-based HTL-free $CH_3NH_3Pb(SCN)_xI_{3-x}$ devices at = 0, 0.0625, 0.125, 0.1875, 0.25 and 0.5, respectively. The fill factor (FF) of these solar cells are 0.52, 0.49, 0.45, 0.46, 0.39 and 0.33 for the carbon-based HTL-free $CH_3NH_3Pb(SCN)_xI_{3-x}$ devices at = 0, 0.0625, 0.125, 0.1875, 0.25 and 0.5, respectively. The $CH_3NH_3PbI_3$ based perovskite solar cells exhibit the highest PCE, 10.74%, among the six conditions. Addition of SCN^- moieties into $CH_3NH_3PbI_3$ structures reduces the $CH_3NH_3Pb(SCN)_xI_{3-x}$ perovskite solar cell efficiencies to 6.34%, 4.43%, 3.84%, 2.41% and 1.55% for x = 0.0625, 0.125, 0.1875, 0.25 and 0.5, respectively. The $CH_3NH_3Pb(SCN)_xI_{3-x}$ (x = 0.0625) perovskite solar cell exhibits most excellent efficiency of all five doping conditions with the efficiency of 6.34%. The $CH_3NH_3Pb(SCN)_xI_{3-x}$ (x = 0.5) perovskite solar cell represented the minimum power conversion efficiency of all five doping conditions. The pure $CH_3NH_3PbI_3$ based perovskite solar cell delivered the highest efficiency among all six different conditions should be due to the smooth, continuous and pinhole-free as seen in the top-view SEM images (figure 38(a)). The XRD spectra of the $CH_3NH_3PbI_3$ film shows the sharp diffraction peaks of the tetragonal $CH_3NH_3PbI_3$ perovskite structure without the appearance of residual precursor peak. Moreover, UV-VIS spectra of the pure $CH_3NH_3PbI_3$ film displays the highest absorbance intensity among all six conditions. Therefore, the suppressed performance of the carbon-based HTL-free $CH_3NH_3Pb(SCN)_xI_{3-x}$ devices should be attributed to the presence of the residual PbI_2 as detected by XRD (Figure 41), decreasing absorbance values as seen in UV-VIS spectra (Figure 42(a)) and increasing the numbers of pinholes and film roughness as presented in Top-view SEM images (Figure 38).

Table 3 the output parameters of the carbon-based HTL-free MAPb(SCN)$_x$I$_{3-x}$ perovskite solar cells.

Perovskite solar cells	Output parameters			
	J_{SC} (mA/cm^2)	V_{OC} (V)	*FF*	η (%)
$CH_3NH_3PbI_3$	21.59	0.95	0.52	10.74
$CH_3NH_3Pb(SCN)_{0.0625}I_{2.9375}$	16.52	0.79	0.49	6.34
$CH_3NH_3Pb(SCN)_{0.125}I_{2.875}$	12.64	0.78	0.45	4.43
$CH_3NH_3Pb(SCN)_{0.1875}I_{2.8125}$	10.15	0.82	0.46	3.84
$CH_3NH_3Pb(SCN)_{0.25}I_{2.75}$	10.60	0.59	0.39	2.41
$CH_3NH_3Pb(SCN)_{0.5}I_{2.5}$	7.84	0.60	0.33	1.55

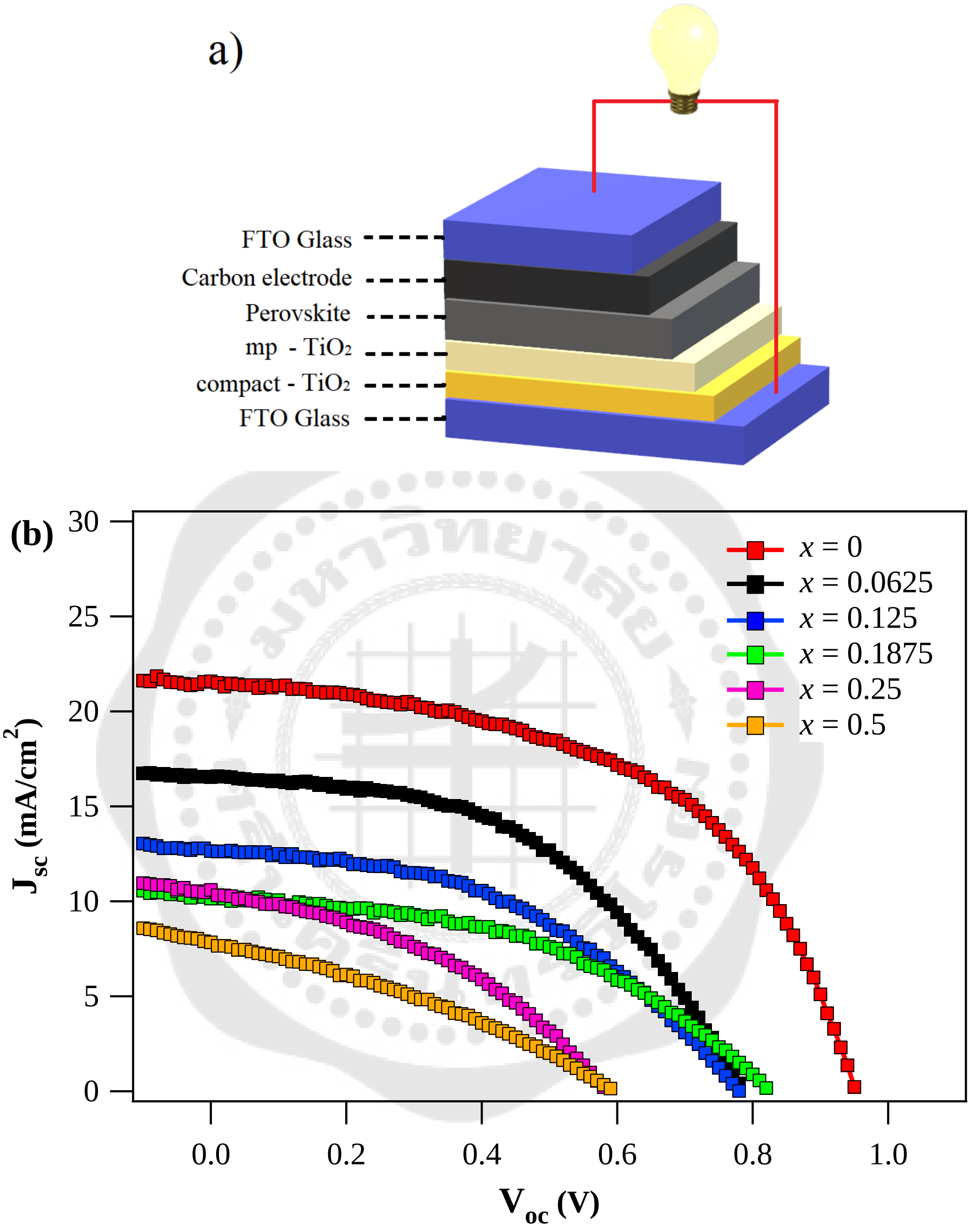

Figure 44 (a) The architecture of the carbon-based HTL-free $CH_3NH_3Pb(SCN)_xI_{3-x}$ perovskite solar cells and (b) the J-V curves of the carbon-based HTL-free $CH_3NH_3Pb(SCN)_xI_{3-x}$ perovskite solar cells of the 1st day.

4.2.2 Stability of $CH_3NH_3Pb(SCN)_xI_{3-x}$ perovskite solar cells

The stabilities of the $CH_3NH_3Pb(SCN)_xI_{3-x}$ perovskite solar cells were tested for 30 days, and the stabilities of power conversion efficiency (PCE), short circuit current density (J_{sc}), open circuit voltage (V_{oc}) and Fill factor (*FF)* are presented in Figure. 45(a-d), and are listed in Table 4. During the stability measurements, devices were stored under ambient air with humidity of 50-60%. It can be seen from Figure 45(a) that the efficiency of the pure $CH_3NH_3PbI_3$ (x = 0) perovskite solar cell significantly dropped from the first day onward (from 10.74% to 2.89%). Only 26.91% of its initial output remained after 30 days. Surprisingly, all $CH_3NH_3Pb(SCN)_xI_{3-x}$ (x = 0.0625, 0.125, 0.1875, 0.25 and 0.5) perovskite solar cells retained their PCEs, over 70% of their initial values after 30-days of testing, as seen in Figure. 45(a). The PCE of $CH_3NH_3Pb(SCN)_xI_{3-x}$ (x = 0.0625) perovskite solar cell dropped to 5.04% on day 30 in comparing to the initial value of 6.34%, which remained 79.43% of the initial efficiency. The $CH_3NH_3Pb(SCN)_xI_{3-x}$ (x = 0.5) perovskite solar cell represented the minimum power conversion efficiency of all five doping conditions, but the PCE only decreased 16.22% from the initial PCE (from 1.55% to 1.30%). The short circuit current density (J_{sc}) and Fill factor (FF) of pure $CH_3NH_3PbI_3$ (x = 0) perovskite solar cell obviously plunged after 30 days of testing. On the other hand, the short circuit current density (J_{sc}) and Fill factor (FF) of all $CH_3NH_3Pb(SCN)_xI_{3-x}$ (x = 0.0625, 0.125, 0.1875, 0.25 and 0.5) perovskite solar cells remained constant. The open circuit voltage (V_{oc}) of all six conditions likely attended to be steady. This suggest that, the efficiency reduction of the pure $CH_3NH_3PbI_3$ solar cell is mainly caused by a decrease of J_{sc} and *FF*, as seen in Figure. 45(b) and 45(d). The normalized efficiency curves of the carbon-based HTL-free $CH_3NH_3Pb(SCN)_xI_{3-x}$ perovskite solar cells in Figure. 46 show significant stability of the $CH_3NH_3Pb(SCN)_xI_{3-x}$ cells compared to a pure $MAPbI_3$ perovskite solar cell. J_{sc}, V_{oc} and *FF* values of the $CH_3NH_3Pb(SCN)_xI_{3-x}$ perovskite solar cells also exhibit good stability for 30 days. This suggest that a small introduction of SCN^- moieties into a $CH_3NH_3Pb(SCN)_xI_{3-x}$ perovskite film, as low as x = 0.0625, could greatly enhance film stability.

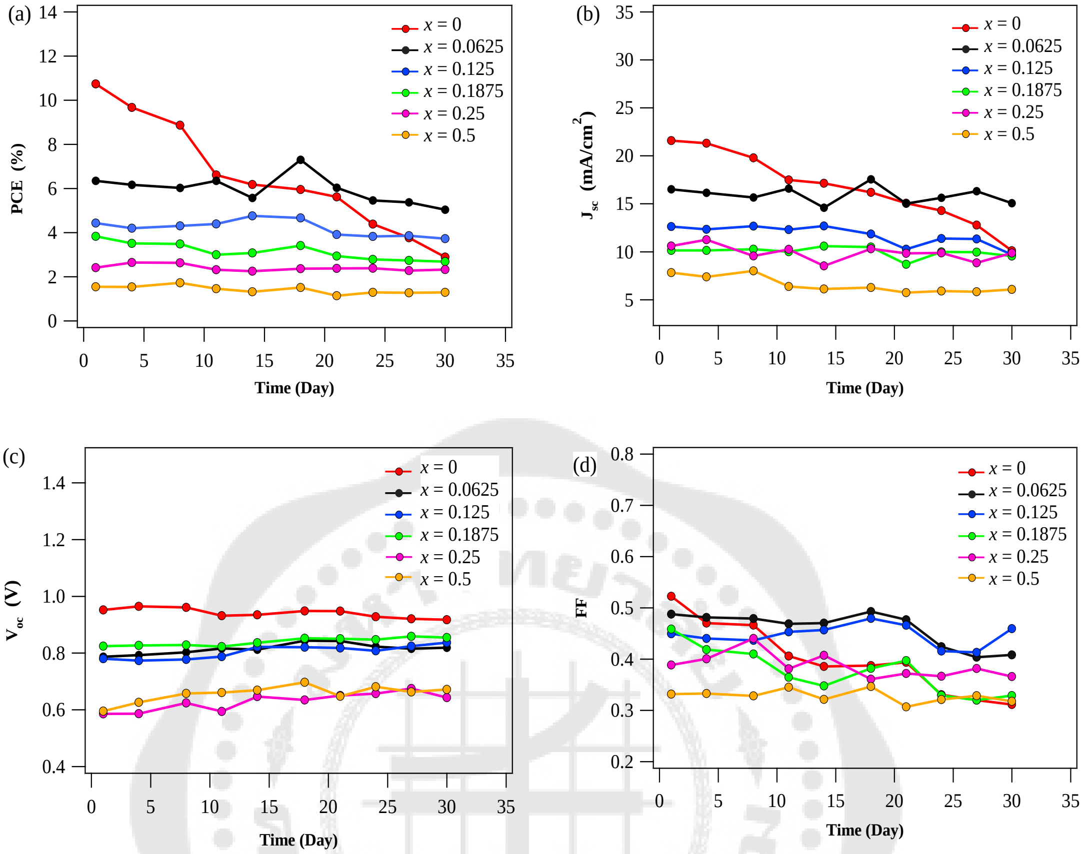

Figure 45 (a) PCE, (b) J_{sc}, (c) V_{oc} and (d) *FF* versus time (in days) of the carbon-based HTL-free $MAPb(SCN)_xI_{3-x}$ perovskite solar cells.

Table 4 The comparison of solar cells parameters between day 1 and day 30

Conditions	Days	J_{SC} (mA/cm^2)	V_{OC} (V)	FF	η (%)
$CH_3NH_3PbI_3$	0	21.59	0.95	0.52	10.74
	30	10.12	0.91	0.31	2.79
$CH_3NH_3Pb(SCN)_{0.0625}I_{2.9375}$	0	16.52	0.79	0.49	6.34
	30	15.07	0.82	0.41	5.04
$CH_3NH_3Pb(SCN)_{0.125}I_{2.875}$	0	12.64	0.78	0.45	4.43
	30	9.70	0.84	0.46	3.73
$CH_3NH_3Pb(SCN)_{0.1875}I_{2.8125}$	0	10.15	0.82	0.46	3.84
	30	9.55	0.85	0.33	2.69
$CH_3NH_3Pb(SCN)_{0.25}I_{2.75}$	0	10.60	0.59	0.39	2.41
	30	9.87	0.64	0.37	2.32
$CH_3NH_3Pb(SCN)_{0.5}I_{2.5}$	0	7.84	0.60	0.33	1.55
	30	6.07	0.67	0.32	1.30

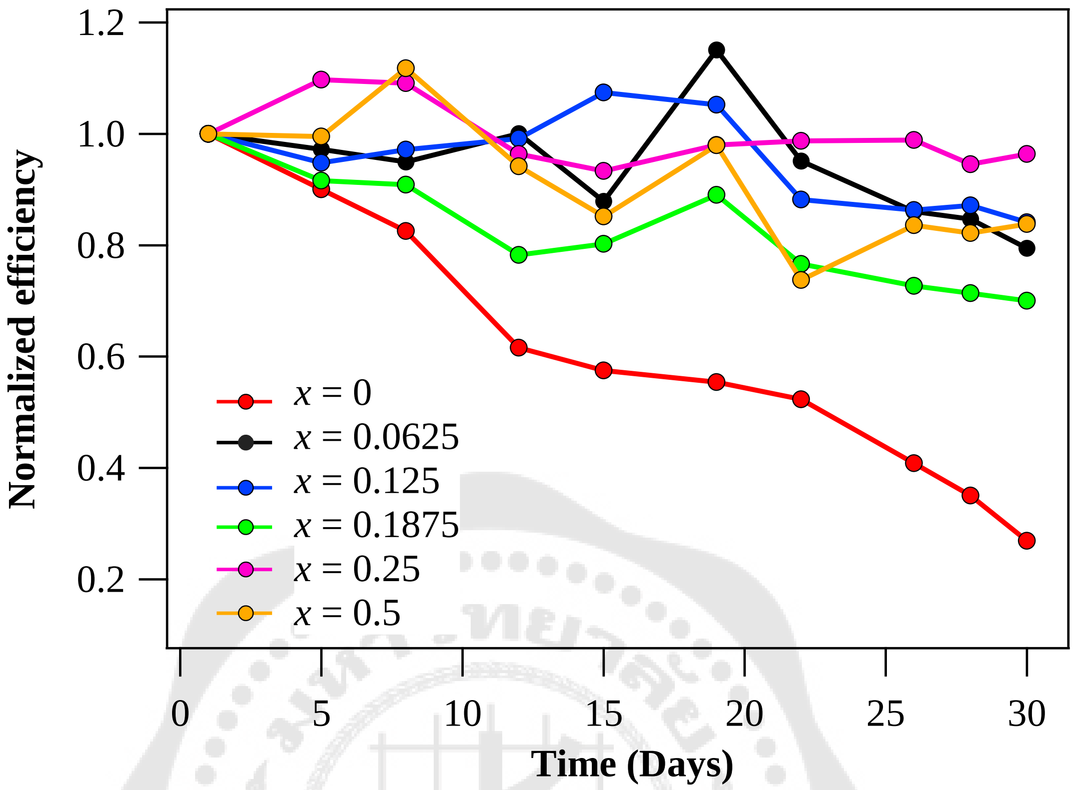

Figure 46 The normalized efficiency of the carbon-based HTL-free $MAPb(SCN)_xI_{3-x}$ perovskite solar cells with respected to their first day values.

CHAPTER 5

SUMMARY DISCUSSION AND SUGGESTION

5.1 Summary

In this work, we assembled the low-cost perovskite solar cells and improved the $CH_3NH_3PbI_3$ film stability by doping SCN^- moiety. The $CH_3NH_3Pb(SCN)_xI_{3-x}$ perovskite films were deposited on the TiO_2 film using one-step deposition and hot-casting method with six different $Pb(SCN)_2$ concentrations (x = 0, 0.0625, 0.125, 0.1875, 0.25 and 0.25). The morphology, optical and crystallinity of the prepared $CH_3NH_3Pb(SCN)_xI_{3-x}$ perovskite films were studied via scanning electron microscope (SEM), UV-VIS spectroscopy and X-Ray diffraction spectroscopy, respectively. Afterwards, the carbon-based hole-transport-layer-free $CH_3NH_3Pb(SCN)_xI_{3-x}$ perovskite solar cells were assembled and characterized. The results of this research is summarized as follow.

5.1.1 The effects of $Pb(SCN)_2$ moiety on $CH_3NH_3PbI_3$ morphology, crystallinity and absorbance.

This study found that the concentrations of 0.0625 M, 0.125 M and 0.1875 M $Pb(SCN)_2$ additions would enlarge the grain-size of perovskite film. However, the high concentrations of 0.25 M and 0.5 M $Pb(SCN)_2$ additions would build the rodlike shape on the film surfaces. The diffraction peaks of the pure $CH_3NH_3PbI_3$ (0 M $Pb(SCN)_2$) film appear at 14.14°, 28.47° and 31.90° corresponded to the (110), (220) and (310) planes of a tetragonal $CH_3NH_3PbI_3$ structure, respectively. XRD spectra of the 0.0625 M, 0.125 M, 0.1875 M, 0.25 M and 0.5 M $Pb(SCN)_2$ added films also appear at 14.11°, 28.44° and 31.88°, and the sharp peak of residual PbI_2 precursor at 12.66°. Moreover, the UV-VIS spectra of the 0.0625 M, 0.125 M, 0.1875 M, 0.25 M and 0.5 M $Pb(SCN)_2$ added films presented two different absorbance edge at 780-790 nm (the $CH_3NH_3PbI_3$ absorbance edge) and at 530-540 nm (the PbI_2 absorbance edge). However, the pure $CH_3NH_3PbI_3$ (0 M $Pb(SCN)_2$) film only present the absorbance edge at 780-790 nm. The XRD and UV-VIS spectra suggest that the increasing $Pb(SCN)_2$ addition induces the second phase PbI_2 formation on the perovskite film.

5.1.2 The effects of $Pb(SCN)_2$ moiety on the carbon-based hole-transport-layer-free perovskite solar cells

The performances of carbon-based hole-transport-layer-free perovskite solar cell shows that the optimum power conversion efficiency (PCE) is obtained from the pure $CH_3NH_3PbI_3$ (0 M $Pb(SCN)_2$) solar cell with the efficiency of 10.74%. The increasing $Pb(SCN)_2$ concentration would lower the solar calls power conversion efficiency (PCE), and the lowest concentration 0.0625 M $Pb(SCN)_2$ represents the highest PCE of 6.34%. The PCE decreases with the Pb(SCN)2 added ratios, which should relate to the PbI_2 formation as detected in XRD spectra. However, the stability of the pure $CH_3NH_3PbI_3$ (0 M $Pb(SCN)_2$) solar cell significantly dropped from 10.74% to 2.79% after 30 days testing, which is only 25.98% of the initial PCE. On the other hand, the additive $Pb(SCN)_2$ solar cells exhibit the great solar cell stability with PCE retention of 70% of their initial values after 30 days testing for all conditions.

5.2 Discussion

In this study, we focused our attention on synthesizing perovskite films and investigating the influence of low $Pb(SCN)_2$ added concentration at 0.0625 M, 0.125 M, 0.1875 M, 0.25 M and 0.5 M on the $CH_3NH_3PbI_3$ perovskite film morphology, crystallinity and absorption, as well as on the performance of carbon-based HTL-free perovskite solar cells. In order to understand the effects of $Pb(SCN)_2$ addition on the perovskite films on morphology and crystallites, all the perovskite films condition were analyzed by SEM, XRD and UV-VIS technique. The finding indicates that the introduction of $Pb(SCN)_2$ can enlarge grainsize of the films as seen in Top-view of SEM images (Figure 38.). Another important findings of this work is that the $Pb(SCN)_2$ addition induced the sharp peak at 12.66°, which is due to the PbI_2 film formation on the prepared films as seen in Figure 41. The absorbance edge at 530-540 nm is belonging to the PbI_2 absorbance edge as shown in Figure 42(a). The formation of PbI_2 secondary phase on the $Pb(SCN)_2$ added films was reported by many groups. (Weijun Ke & Dewei Zhao 2016) proposed that the SCN-moiety interacted with $CH_3NH_3^+$ moiety becoming HSCN and CH_3NH_2 gases during the film annealing process. This would lead to the over remaining of PbI_2 (i.e. the PbI2/MAI ratio over 1) on the substrate, which is subsequently converting into the second phase PbI_2 as illustrated in below Equation

$$\mathrm{CH_3NH_3I}+(1-\mathrm{x})\mathrm{PbI_2}+(\mathrm{x})\mathrm{Pb}(\mathrm{SCN})_2\rightarrow(1-2\mathrm{x})\mathrm{CH_3NH_3PbI_3}+(2\mathrm{x})\mathrm{PbI_2}+(2\mathrm{x})\mathrm{HSCN}(\mathrm{g})+(2\mathrm{x})\mathrm{CH_3NH_2}(\mathrm{g})$$

From the above Equation implies that the high $Pb(SCN)_2$ dopant would cause more PbI_2 formation on the prepared samples. Intensity of XRD peak at 12.66° in Figure 41 greatly increases with the $Pb(SCN)_2$ added levels. This implies that $Pb(SCN)_2$ addition hindered the chemical reaction between CH_3NH_3I and PbI_2 that lowering the perovskite solar cell efficiency.

All six prepared perovskite films were used as a light absorption layer in carbon-based HTL-free perovskite solar cells. The architecture of these carbon-based HTL-free solar cells consists of FTO/compact-TiO_2/mp-TiO_2/perovskite/carbon/FTO, as illustrated in Figure 44(a). In order to study the performances of these carbon-based HTL-free perovskite solar cells, all of the devices were measured under a simulated sunlight intensity of 100 $mWcm^{-2}$ at 1.5 AM. The pure $CH_3NH_3PbI_3$ (0M-$Pb(SCN)_2$) based perovskite solar cells exhibit the highest PCE, 10.74%, among the six conditions. Addition of SCN- moieties in building the $CH_3NH_3PbI_3$ structures reduces the efficiencies to 6.34%, 4.43%, 3.84%, 2.41% and 1.55% for $Pb(SCN)_2$ at 0.0625 M, 0.125 M, 0.1875 M, 0.25 M and 0.5 M respectively. The suppressed performance is attributed to the increasing the numbers of pinholes and film roughness as represented in SEM images (Figure. 41), the decreasing absorbance values as seen in UV-VIS spectra (Figure 42(a)) and the presence of PbI_2 phases as detected by XRD (Figure 44), However, the good stability of the $Pb(SCN)_2$ addition perovskite solar cell were obtained because there is a PbI_2 layer minimizing oxygen and/or water molecules penetration to degrade $CH_3NH_3PbI_3$ perovskite film.

5.3 Suggestions

The air temperature and humidity during the solar cell fabrication should be controlled because the perovskite film in our work is sensitive to moisture. The annealing temperature is also the important key to the morphology and perovskite formation. Thus, all tools and equipment should be clean very neatly and accurately in order to obtain the best perovskite film quality.

REFERENCES

Bu, F., He, B., Ding, Y., Li, X., Sun, X., Duan, J., . . . Tang, Q. (2020). Enhanced energy level alignment and hole extraction of carbon electrode for air-stable hole-transporting material-free CsPbBr3 perovskite solar cells. *Solar Energy Materials and Solar Cells, 205*, 110267. doi:https://doi.org/10.1016/j.solmat.2019.110267

Cai, Y., Wang, S., Sun, M., Li, X., & Xiao, Y. (2018). Mixed cations and mixed halide perovskite solar cell with lead thiocyanate additive for high efficiency and long-term moisture stability. *Organic Electronics, 53*, 249-255. doi:https://doi.org/10.1016/j.orgel.2017.11.045

Chen, Y., Li, B., Huang, W., Gao, D., & Liang, Z. (2015). Efficient and reproducible CH3NH3PbI3−x(SCN)x perovskite based planar solar cells. *Chemical communications, 51*(60), 11997-11999. doi:10.1039/C5CC03615A

Chiang, C.-H., Lin, J.-W., & Wu, C.-G. (2016). One-step fabrication of a mixed-halide perovskite film for a high-efficiency inverted solar cell and module. *Journal of Materials Chemistry A, 4*(35), 13525-13533. doi:10.1039/C6TA05209F

Di Giacomo, F., Fakharuddin, A., Jose, R., & Brown, T. M. (2016). Progress, challenges and perspectives in flexible perovskite solar cells. *Energy & Environmental Science, 9*(10), 3007-3035. doi:10.1039/C6EE01137C

Elumalai, N. K., Mahmud, M. A., Wang, D., & Uddin, A. (2016). Perovskite Solar Cells: Progress and Advancements. *Energies, 9*, 861. doi:10.3390/en9110861

Gong, S., Li, H., Chen, Z., Shou, C., Huang, M., & Yang, S. (2020). CsPbI2Br Perovskite Solar Cells Based on Carbon Black-Containing Counter Electrodes. *ACS Applied Materials & Interfaces, 12*(31), 34882-34889. doi:10.1021/acsami.0c08006

Halder, A., Chulliyil, R., Subbiah, A. S., Khan, T., Chattoraj, S., Chowdhury, A., & Sarkar, S. K. (2015). Pseudohalide (SCN–)-Doped MAPbI3 Perovskites: A Few Surprises. *The Journal of Physical Chemistry Letters, 6*(17), 3483-3489. doi:10.1021/acs.jpclett.5b01327

Jenny Nelson. (2003). *The Physics of Solar Cells*. London: Imperial College Press.

Jiang, Q., Rebollar, D., Gong, J., Piacentino, E. L., Zheng, C., & Xu, T. (2015). Pseudohalide-induced moisture tolerance in perovskite CH3 NH3 Pb(SCN)2 I thin films. *Angew Chem Int Ed Engl, 54*(26), 7617-7620. doi:10.1002/anie.201503038

Jiang, Q., Rebollar, D., Gong, J., Piacentino, E. L., Zheng, C., & Xu, T. (2015). Pseudohalide-Induced Moisture Tolerance in Perovskite CH3NH3Pb(SCN)2I Thin Films. *Angewandte Chemie International Edition, 54*(26), 7617-7620. doi:https://doi.org/10.1002/anie.201503038

Ke, W., Xiao, C., Wang, C., Saparov, B., Duan, H.-S., Zhao, D., . . . Yan, Y. (2016). Employing Lead Thiocyanate Additive to Reduce the Hysteresis and Boost the Fill Factor of Planar Perovskite Solar Cells. *Advanced Materials, 28*(26), 5214-5221. doi:https://doi.org/10.1002/adma.201600594

Kim, M. K., Jeon, T., Park, H. I., Lee, J. M., Nam, S. A., & Kim, S. O. (2016). Effective control of crystal grain size in CH3NH3PbI3 perovskite solar cells with a pseudohalide Pb(SCN)2 additive. *CrystEngComm, 18*(32), 6090-6095. doi:10.1039/C6CE00842A

Kim, T., Lim, J., & Song, S. (2020). Recent Progress and Challenges of Electron Transport Layers in Organic–Inorganic Perovskite Solar Cells. *Energies, 13*(21), 5572.

Kumlangwan, P., Suksangrat, P., Towannang, M., Faibut, N., Harnchana, V., Srepusharawoot, P., . . . Amornkitbamrung, V. (2020). Calculation and Fabrication of a CH3NH3Pb(SCN)xI3−x Perovskite Film as a Light Absorber in Carbon-based Hole-transport-layer-free Perovskite Solar Cells. *Journal of the Korean Physical Society, 77*(12), 1210-1217. doi:10.3938/jkps.77.1210

Kumlanwan, P., Suksangra, P., Towannang, M., Faibut, N., Chompoosor, A., Kumnorkaew, P., . . . Amornkitbamrung, V. (2020). Calculation and Fabrication of a CH3NH3Pb(SCN)xI3-x Perovskite Film as a Light Absorber in Carbon-based Hole-transport-layer-free Perovskite Solar Cells. *the Korean Physical Society, 77*, 1-8.

Liu, T., Wang, Z., Lou, L., Xiao, S., Zheng, S., & Yang, S. (2020). Interfacial Post-Treatment for Enhancing the Performance of Printable Carbon-Based Perovskite Solar Cells. *Solar RRL, 4*(2), 1900278. doi:https://doi.org/10.1002/solr.201900278

Lou, Y., Niu, Y., Yang, D., Xu, Q., Hu, Y., Shen, Y., . . . Zhao, Y. (2018). Rod-shaped thiocyanate-induced abnormal band gap broadening in SCN$^-$ doped CsPbBr3 perovskite nanocrystals. *Nano Research, 11*(5), 2715-2723. doi:10.1007/s12274-017-1901-z

O'Regan, B., & Grätzel, M. (1991). A low-cost, high-efficiency solar cell based on dye-sensitized colloidal TiO2 films. *Nature, 353*(6346), 737-740. doi:10.1038/353737a0

Shi, Z., & Jayatissa, A. H. (2018). Perovskites-Based Solar Cells: A Review of Recent Progress, Materials and Processing Methods. *Materials (Basel), 11*(5). doi:10.3390/ma11050729

Tai, Q., You, P., Sang, H., Liu, Z., Hu, C., Chan, H. L. W., & Yan, F. (2016). Efficient and stable perovskite solar cells prepared in ambient air irrespective of the humidity. *Nature communications, 7*(1), 11105. doi:10.1038/ncomms11105

Wang, G., Liu, D., Xiang, J., Zhou, D., Alameh, K., Ding, B., & Song, Q. (2016). Efficient perovskite solar cell fabricated in ambient air using one-step spin-coating. *RSC Advances, 6*(49), 43299-43303. doi:10.1039/C6RA05893K

Weijun Ke , C. X., Changlei Wang , Bayrammurad Saparov , Hsin-Sheng Duan ,, & Dewei Zhao , Z. X., ... , Yanfa Yan. (2016). Employing Lead Thiocyanate Additive to Reduce the Hysteresis and Boost the Fill Factor of Planar Perovskite Solar Cells. *advance materials, 28*, 5214–5221.

Yu, Y., Wang, C., Grice, C. R., Shrestha, N., Zhao, D., Liao, W., . . . Yan, Y. (2017). Synergistic Effects of Lead Thiocyanate Additive and Solvent Annealing on the Performance of Wide-Bandgap Perovskite Solar Cells. *acs energy letters, 2*(5), 1177-1182. doi:10.1021/acsenergylett.7b00278

Zhao, Y., & Zhu, K. (2014). CH3NH3Cl-Assisted One-Step Solution Growth of CH3NH3PbI3: Structure, Charge-Carrier Dynamics, and Photovoltaic Properties of Perovskite Solar Cells. *The Journal of Physical Chemistry C, 118*(18), 9412-9418. doi:10.1021/jp502696w

ดนัย กิจชัยนุกูล. (2547). เรื่องน่ารู้ของกล้องจุลทรรศน์อิเล็กตรอนแบบส่องกราด (Scanning Electron microscope : SEM). Retrieved 14/06/2020 https://soreda.oas.psu.ac.th/files/944_file_Chapter4.pdf

ธิติ มหาเจริญ. (2561). การตรวจลักษณะทางพื้นผิวและธาตุองค์ประกอบในเส้นใยสังเคราะห์ และเส้นใยธรรมชาติที่พบในประเทศไทยโดยวิธี *Scanning Electron Microscope/Dispersive X-ray Spectroscopy* เพื่อประยุกต์ใช้ในงานนิติวิทยาศาสตร์. โรงเรียนนายร้อยตำรวจ,

พรรณธิวา, ก. (2562). การประดิษฐ์ฟิล์มบาง *CH3NH3Pb(SCN)2I1* สำหรับใช้เป็นตัวดูดกลืนแสงในระบบเซลล์แสงอาทิตย์แบบเพอรอฟสไกต์ (ปริญญาวิทยาศาสตรมหาบัณฑิต), มหาวิทยาลัยขอนแก่น, ขอนแก่น.

สมัคร์, พ. (2556). ทฤษฎีเซลล์แสงอาทิตย์เบื้องต้น. ขอนแก่น: ภาควิชาฟิสิกส์, มหาวิทยาลัยขอนแก่น.


มหาวิทยาลัย
ศรีนครินทรวิโรฒ

VITA

NAME	Primprapha Prasan
DATE OF BIRTH	13 December 1993
PLACE OF BIRTH	Yasothon
HOME ADDRESS	45 Chaosadet street, Namkhamyai dr, Mueang Yasothon, Yasothon, 35000.